Coupling ecological concepts with an ocean-colour model: Parameterisation and forward modelling

Xuerong Sun [a],[*], Robert J.W. Brewin [a], Shubha Sathyendranath [b],[c], Giorgio Dall'Olmo [d],
David Antoine [e],[f], Ray Barlow [g], Astrid Bracher [h],[i], Malika Kheireddine [j], Mengyu Li [k],
Dionysios E. Raitsos [l], Fang Shen [k], Gavin H. Tilstone [b], Vincenzo Vellucci [f],[m]

[a] Centre for Geography and Environmental Science, Department of Earth and Environmental Sciences, Faculty of Environment, Science and Economy, University of Exeter, Cornwall, United Kingdom
[b] Plymouth Marine Laboratory, Plymouth, Devon, United Kingdom
[c] National Centre for Earth Observation, Plymouth Marine Laboratory, Plymouth, Devon, United Kingdom
[d] Istituto Nazionale di Oceanografia e di Geofisica Sperimentale - OGS, Trieste, Italy
[e] Remote Sensing and Satellite Research Group, School of Earth and Planetary Sciences, Curtin University, Perth, Australia
[f] Sorbonne Université, CNRS, Institut de la Mer de Villefranche, IMEV, Villefranche-sur-Mer, France
[g] Bayworld Centre for Research & Education, Cape Town, South Africa
[h] Phytooptics, Alfred Wegener Institute, Helmholtz Centre for Polar and Marine Research, Bremerhaven, Germany
[i] Institute of Environmental Physics, University of Bremen, Bremen, Germany
[j] King Abdullah University of Science and Technology (KAUST), Red Sea Research Center (RSRC), Biological and Environmental Sciences & Engineering Division (BESE), Bioscience program, Thuwal, Saudi Arabia
[k] State Key Laboratory of Estuarine and Coastal Research, East China Normal University, Shanghai, China
[l] Department of Biology, National and Kapodistrian University of Athens, Athens, Greece
[m] Sorbonne Université, CNRS, OSU Station Marines, STAMAR, Paris, France

ARTICLE INFO

ABSTRACT

In the first part of this paper series (Sun et al., 2023), we developed an ecological model that partitions the total chlorophyll-a concentration (Chl-a) into three phytoplankton size classes (PSCs), pico-, nano-, and microplankton. The parameters of this model are controlled by sea surface temperature (SST), intended to capture shifts in phytoplankton size structure independently of variations in total Chl-a. In this second part of the series, we present an Ocean Colour Modelling Framework (OCMF), building on the classical Case-1 assumption, that explicitly incorporates our ecological model. The OCMF assumes the presence of the three PSCs and the existence of an independent background of non-algal particles. The framework assumes each phytoplankton group resides in a distinct optical environment, assigning chlorophyll-specific inherent optical properties to each group, both directly (phytoplankton) and indirectly (non-algal particulate and dissolved substances). The OCMF is parameterised, validated, and assessed using a large global dataset of inherent and apparent optical properties. We use the OCMF to explore the influence of variations in temperature and Chl-a on phytoplankton size structure and its resulting effects on ocean colour. We also discuss applications of the OCMF, such as its potential for inverse modelling and phytoplankton climate trend detection, which will be explored further in subsequent papers.

1. Introduction

Changes in the Earth's climate are driving alterations in phytoplankton biomass, type, and phenology in marine ecosystems (Boyce et al., 2010; Ardyna and Arrigo, 2020; Thomalla et al., 2023), with significant impacts on the food web, biogeochemical cycles, and primary production (Richardson and Schoeman, 2004; Litchman et al., 2015; Lewis et al., 2020). Studying these alterations requires suitable monitoring systems. Ocean-colour remote sensing serves as the only available tool providing near real-time information on phytoplankton in the surface ocean under natural conditions at synoptic scales (Krug et al., 2017). The continuous global ocean colour data record has now exceeded 27 years, creating an invaluable resource that is suitable in length (at least in some areas of the ocean) for studying and understanding

long-term changes in marine ecosystems (Hammond et al., 2020). Recent improvements in the stability and consistency of ocean colour measurements (Werdell et al., 2009; Mélin et al., 2017; Sathyendranath et al., 2019) have made them the primary data source for evaluating the response of phytoplankton to climate change (McClain, 2009; Dutkiewicz et al., 2019; Cael et al., 2023). Every day, a vast amount of ocean colour data, represented by remote sensing reflectances (R_{rs}), are collected and available for interpreting the optical properties of waters. The foundational step is to understand how to describe the R_{rs} signal, known as R_{rs} forward modelling (Sathyendranath et al., 2000).

Forward modelling in ocean optics involves predicting R_{rs} from optically active substances. The magnitude and shape of R_{rs} are determined by the inherent optical properties (IOPs) of these substances, including the absorption (a) and backscattering (b_b) coefficients of phytoplankton, non-algal particles (NAP), coloured dissolved organic matter (CDOM), and seawater (Zaneveld et al., 2006). In other words, the key aspect of the forward modelling is to quantitatively infer R_{rs} from a and b_b. The two components of this process are the relationship between biogeochemical variables and IOPs, and the relationship between the IOPs and the R_{rs}. In this study, we focus on open ocean waters, commonly known as Case-1 waters (Morel and Prieur, 1977), where optical properties covary with chlorophyll-a concentration (Chl-a) (Prieur and Sathyendranath, 1981; Morel, 1988). It implies that optical properties of all non-water constituents are linked to variations in Chl-a. Consequently, the establishment of the relationship between biogeochemical variables and IOPs can be achieved through Chl-a (Bricaud et al., 1998b; Morel and Maritorena, 2001; Reynolds et al., 2001). As for the IOPs and the R_{rs} connection, the latter can be mathematically modelled as a quadratic function of a and b_b, using the quasi single scattering approximation of the radiative transfer equation (Gordon et al., 1988; Lee et al., 1994; Sathyendranath and Platt, 1997). These fundamental concepts form the basis of the forward modelling that we develop in this study.

Due to issues around ambiguity (Defoin-Platel and Chami, 2007), interpreting phytoplankton information using ocean colour data poses a significant challenge (Sun et al., 2023). Phytoplankton diversity is one of the main causes of this issue. For example, the phytoplankton size structure in the water can impact the colour of the ocean, represented by R_{rs}, and the same R_{rs} may correspond to various size compositions and Chl-a concentrations (Brewin et al., 2014; Sathyendranath et al., 2017). This is related to changes in phytoplankton absorption coefficients (a_{ph}), caused by cell size and taxon-specific changes in pigmentation (Hoepffner and Sathyendranath, 1991; Bricaud et al., 2004), which ultimately have an effect on R_{rs} (Taylor et al., 2011a; Uitz et al., 2015; Brewin et al., 2019). To address the ambiguity caused by phytoplankton size, we introduced the effect of sea surface temperature (SST) on the relationship between Chl-a and PSCs (Ward, 2015; Brewin et al., 2017; Sun et al., 2023), which is based on the following considerations. Firstly, the size composition of phytoplankton is influenced by temperature, either directly through the impact on the physiological characteristics of phytoplankton, such as rates of nutrient uptake, or indirectly through its covariation with resource availability, including light and nutrients (López-Urrutia and Morán, 2015; Marañón et al., 2015). Secondly, remotely sensed SST is highly accurate (Minnett et al., 2019), which could serve as an explanatory independent variable useful for enriching our interpretation of ocean colour data and reducing ambiguity (Defoin-Platel and Chami, 2007). Another issue regarding the ambiguity problem concerns non-algal substances and their optical properties, which impact the NAP absorption (a_d), CDOM absorption (a_g), and particulate backscattering (b_{bp}) coefficients. Many investigations have demonstrated that in Case-1 waters, these IOPs can be empirically modelled as a function of Chl-a (Huot et al., 2008; Morel, 2009). Nonetheless, these IOPs are not constant in space and time, may be subject to changes with climate, and can show variability for the same Chl-a concentration (Organelli et al.,

2014; Devred et al., 2022). Changes in the optical properties of non-algal substances for the same phytoplankton biomass and size structure can also result in different R_{rs} (Huot and Antoine, 2016). Therefore, it is essential to develop forward models that accurately represents diverse oceanic environments globally, whilst accounting for potential sources of ambiguity.

Building on a previously developed ecological model (Sun et al., 2023), which explicitly incorporates the dependency of model parameters on temperature, this second work aims to present a new global theoretical Ocean Colour Modelling Framework (OCMF). We compile an extensive global dataset of *in-situ* optical properties, including all the key IOPs (i.e., a_{ph}, a_d, a_g, and b_{bp}) and R_{rs}, each of which is accompanied by concurrent *in-situ* Chl-a and remotely sensed SST data. By applying the SST-dependent phytoplankton size structure model from Sun et al. (2023), the total *in-situ* Chl-a is partitioned into the contributions of PSCs. We then construct IOP models driven by the Chl-a of each PSC, obtaining chlorophyll-specific IOPs for each class applicable on a global scale. We compare and assess the performance of the proposed IOP models with previous research. These IOP models are then assembled to construct a R_{rs} forward model. Validation of the OCMF is performed using multiple independent datasets and compared against existing methods. The OCMF presented here explicitly defines the optical environments of different phytoplankton groups and enriches our interpretation of ocean colour using SST. This approach may ultimately improve our ability to extract ecological information from the ever growing satellite ocean colour record.

2. Data

2.1. In-situ datasets

This section provides information on the *in-situ* datasets used in this study, including data sources, variables, and processing procedures. More details about the *in-situ* datasets are available in Sections S3.1 and S3.2 of the Supplementary. All the abbreviations and symbols are defined in Table A.1 in Appendix A.

2.1.1. Data sources

This study uses 47,295 measurements of optical properties and Chl-a, collected in the global surface ocean between 1994 and 2021 (Fig. 1). The dataset was compiled from various public repositories, including: (1) IMOS (2022) from the AODN (Australian Ocean Data Network) Portal; (2) the time series BOUSSOLE (Bouée pour l'acquisition de Séries Optiques à Long Terme) Project (Antoine et al., 2006, 2008; Golbol et al., 2000); (3) NASA SeaBASS (SeaWiFS Bio-optical Archive and Storage System); (4) NOMAD (NASA bio-Optical Marine Algorithm Dataset, version 2.a, Werdell and Bailey, 2005); and (5) published datasets (Bricaud et al., 1998a; Stramski et al., 2008a; Garaba et al., 2011; Taylor et al., 2011b; Taylor and Bracher, 2012a,b; Moutin and Claustre, 2013; Soppa et al., 2013a,c,b,d; Zielinski et al., 2013; Bracher, 2014a,b; Peeken and Nachtigall, 2014; Bracher et al., 2015; Bracher, 2015; Peeken and Murawski, 2016; Boss et al., 2017; Bracher, 2017a,b; Taylor and Bracher, 2017; Bracher et al., 2018; Gonçalves-Araujo et al., 2018a,b; Liu et al., 2018b,c,a; Bracher, 2019; Bracher and Wiegmann, 2019; Liu et al., 2019c,b,a; Wiegmann et al., 2019; Bracher et al., 2020, 2021b,a,d,f,j,k; Bracher and Taylor, 2021b,a; Bracher and Liu, 2021a,b; Bracher et al., 2021c,l,g,e,i,h,m,n; Kramer et al., 2021; Xi et al., 2021; Bracher and Cheah, 2022; Bracher and Wiegmann, 2022b; Bracher and Röttgers, 2022; Bracher and Wiegmann, 2022a; Valente et al., 2022; Röttgers et al., 2023) from PANGAEA.

Additional measurements included in the *in-situ* dataset were obtained from: (1) the Atlantic Ocean (Atlantic Meridional Transect (AMT) cruises, Dall'Olmo et al., 2012; Brewin et al., 2023a), (2) a dataset compiled by Shubha Sathyendranath and Trevor Platt at the Bedford Institute of Oceanography (Sathyendranath et al., 2001; Devred et al., 2006), (3) the Indian Ocean (Barlow et al., 2008, 2011),
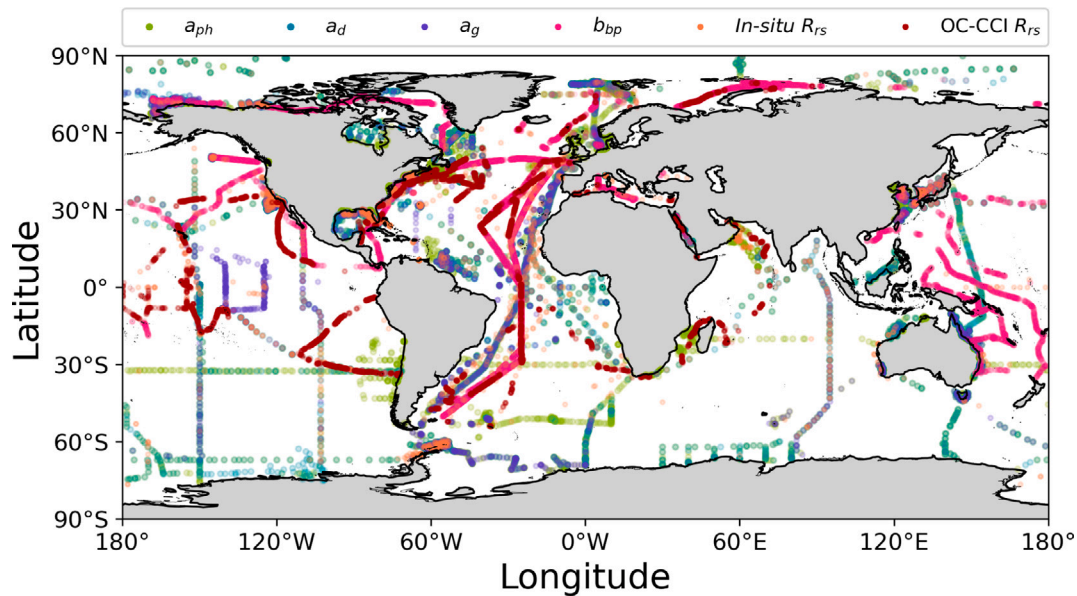
Fig. 1. Locations of *in-situ* datasets used in this study, including six datasets of a_{ph} ($N = 13,988$), a_d ($N = 6758$), a_g ($N = 4639$), b_{bp} ($N = 18,663$), *in-situ* R_{rs} ($N = 3247$), and OC-CCI derived R_{rs} that correspond to the *in-situ* Chl-a measurements from Graban et al. (2020) ($N = 9050$). Note that the data presented here have undergone quality control and data screening procedures. More detailed information on the datasets can be found in Sections 2.1 and 2.3.3, Supplementary Table S1, Supplementary Figures S1-1–S1-6, and Supplementary Section S3.1. (For interpretation of the references to colour in this figure legend, the reader is referred to the web version of this article.)

(4) the Mediterranean Sea (Westberry et al., 2010; Dall'Olmo et al., 2011), (5) the Red Sea (Kheireddine et al., 2018b,a, 2021), (6) the eastern China seas (Sun et al., 2022), (7) the Arctic Ocean (Lewis and Arrigo, 2020), and (8) a global underway bio-optical dataset (Graban et al., 2020).

More detailed information on each public data source, such as website, access time, and the number of samples included, can be found in Section S3.1 of the Supplementary. Supplementary Table S1 provides details of the *in-situ* datasets, including collection dates, study areas, cruise details, contributors' names, and citations.

2.1.2. Data variables and pre-processing procedures

This section presents an overview of data variables used in the study, including the absorption coefficient of phytoplankton ($a_{ph}(\lambda)$), the absorption coefficient of NAP ($a_d(\lambda)$), the absorption coefficient of CDOM ($a_g(\lambda)$), the backscattering coefficient of particles ($b_{bp}(\lambda)$), and the remote sensing reflectance ($R_{rs}(\lambda)$). For each optical property sample, only those with concurrent Chl-a measurements were retained. Four types of Chl-a measurements were used in this study, including those derived from the HPLC (High Performance Liquid Chromatography) method, the *in-vitro* fluorometric method, the line-height method, and the *in-vivo* fluorescence sensor. When multiple sources of Chl-a data were available, HPLC and *in-vitro* fluorometric methods were preferred, with HPLC given the highest priority.

During pre-processing procedures, we applied consistent procedures to all the *in-situ* optical properties, including: (1) analysing each optical property individually with its concurrent Chl-a concentration; (2) restricting the spectral range to 400–700 nm; (3) using IOPs with 1-nm spectral resolution (raw or interpolated) for model development and validation; (4) utilising the water type information derived from OC-CCI satellite data (see Section 2.2 for more information) to filter optical properties for Case-1 open ocean conditions, except the phytoplankton absorption coefficients; (5) removing samples with Chl-a less than 0.001 mg m^{-3}; (6) using samples collected from the upper 20 m of the water column (Montégut et al., 2004); (7) treating multiple observations at the same station but different depths as individual measurements, rather than averaging them; (8) dividing the entire dataset into training and validation datasets according to the sampling

time, specifically before and after 2016, to ensure independence in the validation dataset (Stock and Subramaniam, 2022).

Detailed descriptions of the methods employed for the measurement of optical properties, the spectral resolution of the measurements, and the pre-processing and quality control procedures are provided in Section S3.2 of the Supplementary. A comprehensive overview of each optical dataset, including the spatial and frequency distribution of various attributes, is presented in Supplementary Figures S1-1–S1-6.

2.2. OC-CCI satellite data

Monthly OC-CCI (Ocean Colour Climate Change Initiative) R_{rs} (version 6.0, 4 km resolution, Sathyendranath et al., 2021) were used in this study (https://climate.esa.int/en/projects/ocean-colour/). Water class memberships, specifically 14 optical water classes assigned to each pixel are included in this dataset (Jackson et al., 2017), where classes range from oceanic waters to coastal waters as the number of classes increases. This information was used to identify samples collected in the highly-scattering coastal waters. The OC-CCI monthly R_{rs} data for the past 25 years (1998–2022) were used to identify water classes. For each pixel, the mean values of all 14 classes were calculated, and the class with the highest value was designated as the representative water class for that pixel in that month. Samples (except for a_{ph}) falling into water classes 12, 13, and 14, characterised as turbid coastal waters (Jackson et al., 2017), were excluded prior to analysis.

Daily R_{rs} (4 km resolution, version 6.0) from OC-CCI were also included in this study. This dataset was used to obtain corresponding satellite R_{rs} that match the global *in-situ* Chl-a dataset from Graban et al. (2020) (see Section 2.3.3 and Fig. 1).

2.3. Auxiliary datasets

2.3.1. OISST

Daily OISST (Optimal Interpolation Sea Surface Temperature, version 2, 1/4° resolution), distributed by NOAA PSL, were downloaded from: https://psl.noaa.gov/data/gridded/data.noaa.oisst.v2.highres.html. The OISST is a long-term climate data record containing observations from different platforms, including satellites, ships, buoys and Argo floats. We matched each *in-situ* sample spatially (nearest latitude
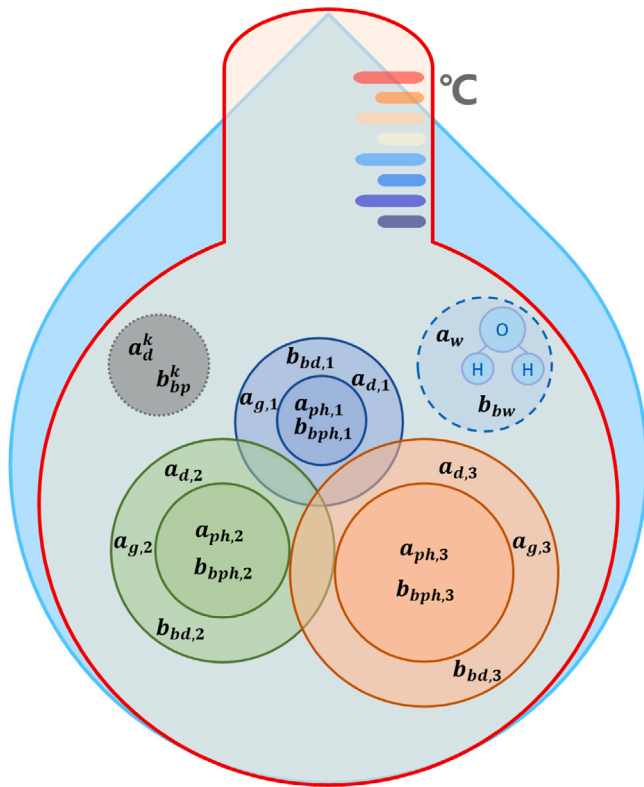
Fig. 2. Schematic of the OCMF. The blue drop represents the ocean and the red thermometer symbolises the inclusion of temperature in the model development. Within the ocean, the dark blue, green, and orange concentric circles are the environments dominated by pico- ($i = 1$), nano- ($i = 2$), and microplankton ($i = 3$), with the inner and outer circles representing the influence of phytoplankton and non-algal substances for each PSC, respectively. The grey dotted and light blue dashed circles illustrate the background of non-algal particles and pure water. The definitions of all relevant IOPs used in this study can be found in the Appendix Table A.1. (For interpretation of the references to colour in this figure legend, the reader is referred to the web version of this article.)

and longitude) and temporally (daily). Only samples with SST values between $-1.8\,°C$ and $40\,°C$ were retained. Due to the lack of concurrent temperature data in many *in-situ* optical datasets, we used daily OISST SST match-ups for model development and validation, which have shown high correlation with *in-situ* measurements in our previous study (see Supplementary Figure S4 in Sun et al. (2023)).

2.3.2. GEBCO gridded bathymetric data

The GEBCO2021 (General Bathymetric Chart of the Oceans), obtained from https://www.gebco.net/data_and_products/gridded_bathymetry_data/#global, was used to extract the bathymetric depth of each *in-situ* sample. We spatially matched each sample to gridded bathymetric data with the nearest latitude and longitude, and retained samples with bathymetric depth below 0 m sea level elevation for further analysis.

2.3.3. A separate validation dataset

The global *in-situ* Chl-a dataset from Graban et al. (2020) was used as an additional dataset to validate the proposed OCMF. It includes *in-situ* Chl-a concentrations estimated from underway a_p using the line-height method (Boss et al., 2007) and de-biased using the Chl-a derived from the HPLC method. Concurrent daily OC-CCI R_{rs} data were matched with *in-situ* Chl-a by pairing each *in-situ* sample in space (3x3 pixel window) and time (daily). The median *in-situ* Chl-a was taken within the 4-km pixel to avoid redundancy. For match-ups with five or more valid pixels out of nine, the median satellite R_{rs} from the

nine pixels surrounding the *in situ* data point was used. The water class information derived from the OC-CCI satellite data was also applied to this dataset (excluding classes 12, 13 and 14), leaving a total of 9050 samples for validation. Note that this dataset is not a fully independent dataset, since samples collected both before 2016 and after 2016 were used, to cover a broader range of samples with varying Chl-a and SST values.

3. Ocean colour modelling framework development

This section introduces the Ocean Colour Modelling Framework (OCMF), mainly based on the classical Case-1 assumption (Morel and Prieur, 1977), that optical properties of the water can be related to Chl-a (Fig. 2). The OCMF incorporates three assemblages of phytoplankton divided by size (i.e., pico- ($< 2\,\mu m$), nano- (2–$20\,\mu m$), microplankton ($> 20\,\mu m$), Sieburth et al., 1978), and assumes the presence of an independent background of NAP. It considers the Chl-a in each size class and how this varies with total Chl-a and SST (Sun et al., 2023). The bio-optical environment representing the dominance of each size class is quantified by assigning chlorophyll-specific IOPs to each size class for each optically active constituent, except that of pure water (Alvain et al., 2012). Where possible, model parameters are designed to be interpretable from a bio-optical or biological perspective. In the following subsections, we describe the components of the OCMF (i.e., SST-dependent size structure and IOPs), model parameterisation, and independent validation. The Pearson linear correlation coefficient (r), p-value (p), coefficient of determination (r^2), bias (δ), mean absolute difference (MAD, ϵ), root mean squared difference (RMSD, ψ), and centre-patterned root mean square difference (Δ), were calculated between measurements and model estimates to evaluate model performance. All statistical test computation equations are given in Supplementary Section S3.3. IOP statistical tests were carried out in $\log_{10}$ space, whereas $R_{rs}(\lambda)$ calculations were made in linear space.

3.1. Three-component models of phytoplankton size structure

We start by considering that the Chl-a within three size classes of phytoplankton, picoplankton (C_1), nanoplankton (C_2) and microplankton (C_3), combine to form the total chlorophyll-a concentration (C), such that,

$$C = \sum_{i=1}^{3} C_i. \tag{1}$$

Brewin et al. (2010) presented a three-component model that relates Chl-a to the three size classes, by defining relationships between C and $C_{1,2}$ (pico- and nanoplankton, $< 20\,\mu m$) and C and C_1,

$$C_{1,2} = C_{1,2}^m [1 - \exp(-\frac{D_{1,2}}{C_{1,2}^m} C)], \tag{2}$$

and

$$C_1 = C_1^m [1 - \exp(-\frac{D_1}{C_1^m} C)], \tag{3}$$

where parameters D determine the fractions of Chl-a as total Chl-a approaches to zero, and parameters C^m are the asymptotic maximum values, respectively. The Chl-a in microplankton (C_3) and nanoplankton (C_2) are calculated as $C_3 = C - C_{1,2}$ and $C_2 = C_{1,2} - C_1$, respectively. By dividing Chl-a of PSCs (C_1, C_2, and C_3) by C, the size fractions (F_i, where $i = 1$, 2, and 3) can be computed.

It has been demonstrated that model parameters in Eqs. (2) and (3) vary predictably with temperature (Ward, 2015; Brewin et al., 2017). Specifically, Brewin et al. (2017) quantified these relationships using a series of logistic functions,

$$C_{1,2}^m = 1 - \left\{ \frac{G_a}{1 + \exp[-G_b(\text{SST} - G_c)]} + G_d \right\}, \tag{4}$$

$$C_1^m = 1 - \left\{ \frac{H_a}{1 + \exp[-H_b(\text{SST} - H_c)]} + H_d \right\}, \tag{5}$$

$$D_{1,2} = \frac{J_a}{1 + \exp[-J_b(\text{SST} - J_c)]} + J_d, \tag{6}$$

and

$$D_1 = \frac{O_a}{1 + \exp[-O_b(\text{SST} - O_c)]} + O_d, \tag{7}$$

where parameters G_i ($i = a - d$), H_i, J_i, and O_i are parameters that control the relationships between $C_{1,2}^m$, C_1^m, $D_{1,2}$, D_1 and SST, respectively. Hereafter, this model was denoted as the 16-parameter model. Additionally, Sun et al. (2023) introduced a new SST-dependent model that relate $C_{1,2}^m$ and C_1^m to SST, according to

$$C_{1,2}^m = U_a \text{SST}^2 + U_b \text{SST} + U_c, \tag{8}$$

and

$$C_1^m = V_a \exp[-(\frac{\text{SST} - V_b}{V_c})^2] + V_d \exp[-(\frac{\text{SST} - V_e}{V_f})^2], \tag{9}$$

where parameters U_i ($i = a - c$) and V_i ($i = a - f$) control the relationships between SST and $C_{1,2}^m$ or C_1^m, respectively. Hereafter, this model was denoted as the 17-parameter model. The parameters and their uncertainties in Eqs. (4)–(9) are taken from our previous study (Sun et al., 2023), as shown in the Table S2 in the Supplementary. The SST-dependent models (i.e., 16- and 17-parameter models) have demonstrated better statistical performance than the SST-independent model using a global dataset (see Table S4 in Sun et al., 2023) and therefore are used in the OCMF. Detailed information on the underlying concepts, development, validation, and discussion of the three-component model can be found in Sun et al. (2023) and references therein.

3.2. Absorption

The absorption coefficient represents the sum of all absorbing components, including particulate (i.e., phytoplankton and NAP) and dissolved (i.e., CDOM) constituents, along with water molecules. In the OCMF, every absorption component can be represented as the product of its Chl-a concentration and its chlorophyll-specific absorption spectrum, with the exception of water and an independent background of NAP.

3.2.1. Absorption by phytoplankton

Phytoplankton absorption, $a_{ph}(\lambda)$, can be modelled as the additive sum of Chl-a in each PSC (C_i) multiplied by its corresponding chlorophyll-specific phytoplankton absorption coefficient ($a_{ph}^*(\lambda)$) (Brewin et al., 2011; Devred et al., 2011), such that,

$$a_{ph}(\lambda) = \sum_{i=1}^{3} a_{ph,i}^*(\lambda) C_i. \tag{10}$$

Using Eq. (10), $a_{ph}^*(\lambda)$ for each size class can be derived, with *in-situ* $a_{ph}(\lambda)$, C, and SST as inputs. Firstly, the size-fractionated Chl-a, C_i, were calculated from C and SST through SST-dependent models (Eqs. (2)–(9)). Secondly, the $a_{ph}^*(\lambda)$ for each size class were derived through minimisation ('lmfit' package in Python) from C_i and $\log_{10}$-transformed $a_{ph}(\lambda)$ data. The results of $a_{ph}^*(\lambda)$ at wavelengths between 400 and 700 nm are shown in Table S3 in the Supplementary. Due to the use of two SST-dependent models (16- and 17-parameter models), there are two sets of size-fractionated Chl-a obtained from a given pair of C and SST, resulting in two sets of specific bio-optical properties for each water constituent. To avoid redundancy, the results derived from the 16-parameter model are presented in the main text, while the results from the 17-parameter model are provided in the Supplementary.

Fig. 3a shows that the a_{ph}^* of picoplankton are the highest, with the steepest spectral shape, followed by nano- and microplankton, which are consistent with many previous findings (Uitz et al., 2008; Bracher et al., 2009; Devred et al., 2011; Kheireddine et al., 2018b). The $a_{ph}^*(\lambda)$ for all the PSCs show two peaks around 440 and 675 nm, related to chlorophyll-a. The variations in shape and magnitude among each

class are due to the size structure and pigment composition (Bracher and Tilzer, 2001; Lohrenz et al., 2003; Kheireddine et al., 2018b). For example, the highest values at blue wavelengths for picoplankton are caused by their small size, and the gradual decrease at 490 nm could be attributed to the pigment zeaxanthin (Barlow et al., 2002). The strong peak at 465 nm in nanoplankton may be due to pigments 19'-butanoyloxyfucoxanthin and 19'-hexanoyloxyfucoxanthin (Jeffrey et al., 2011). The strong package effect in microplankton is the reason for its low values (Sathyendranath et al., 2004). The observed variation in a_{ph}^* within the same size class, indicated by the confidence intervals of the $a_{ph}^*(\lambda)$ obtained through minimisation, can be attributed to the shifts in taxonomic composition (Sun et al., 2022), physiological acclimation of phytoplankton to environmental conditions (e.g., light, temperature, Bouman et al., 2003; Organelli et al., 2017), or spatiotemporal variations in the dataset (Bricaud et al., 1995; Lee et al., 2020).

The retrieved a_{ph}^* were then used to compare the modelled estimates of a_{ph} with observations, using both the parameterisation and independent validation datasets, with Chl-a and SST as inputs. It can be seen that the model functions effectively, as indicated by high correlations (r) and low biases (δ) for six wavelengths covering the visible spectrum (Figs. 3b1–b6). As for the independent validation, the model shows a good performance (Figs. 3c1–c6), with r ranging from 0.859 to 0.917 and ψ from 0.220 to 0.262. A slight overestimation of a_{ph} was observed for all the wavelengths in the independent validation, as indicated by the positive δ, and the highest Δ (0.249) was observed at 560 nm. The validation results align with other research that developed models of a_{ph} as a function of Chl-a and explicitly considering size structure (Devred et al., 2006; Zhang et al., 2015; Brewin et al., 2019). The two SST-dependent models show little differences on the retrieved a_{ph}^* and the validation statistics (see Fig. 3 and Figure S2 in Supplementary). The proposed a_{ph} model was compared with previous models (Bricaud et al., 1995; Brewin et al., 2011), demonstrating improved accuracy (see Section S3.4.1 in Supplementary for details).

3.2.2. Absorption by NAP

NAP absorption, $a_d(\lambda)$, can be modelled as additive sum of Chl-a in each PSC (C_i) multiplied by the chlorophyll-specific NAP absorption coefficient ($a_d^*(\lambda)$). Different from Eq. (10) for phytoplankton, we made the assumption that a background of NAP exists in the ocean (Stramski et al., 2001; Dupouy, 2003), such that,

$$a_d(\lambda) = \sum_{i=1}^{3} a_{d,i}^*(\lambda) C_i + a_d^k(\lambda), \tag{11}$$

where $a_d^k(\lambda)$ represents the a_d for the background. The $a_d(\lambda)$ has a spectral shape that decreases exponentially with wavelength (Roesler et al., 1989), and therefore, Eq. (11) can be further written as

$$a_d(\lambda) = \sum_{i=1}^{3} a_{d,i}^*(\lambda_0) C_i \exp[-S_{d,i}(\lambda - \lambda_0)] + a_d^k(\lambda_0)\exp[-S_d^k(\lambda - \lambda_0)], \tag{12}$$

where $S_{d,i}$ represents the slope of exponent for each PSC (C_i), the S_d^k represents the slope of the exponent for the background, and the reference wavelength λ_0 is 440 nm. The $a_{d,i}^*(\lambda_0)$ and $S_{d,i}$ for each size class, as well as $a_d^k(\lambda_0)$ and S_d^k for the background, were derived through minimisation ('lmfit' package in Python) from C_i (calculated from C and SST through Eqs. (2)–(9)) and $\log_{10}$-transformed $a_d(\lambda)$ data. The parameters are provided in Table S4 in the Supplementary.

The two SST-dependent models show distinct influences on the retrieval results (Fig. 4a and Figure S3a in Supplementary). However, similar trends in magnitude were observed for the three size classes, with nanoplankton showing the highest $a_d^*(\lambda_0)$, followed by pico- and microplankton. As for the slope S_d, picoplankton shows the highest value, followed by micro- and nanoplankton. When the 17-parameter model was employed, a more noticeable spectral dependency was seen across different size classes. The S_d values are in line with the range found in oceanic waters (Babin et al., 2003; Bricaud et al., 2010; Devred
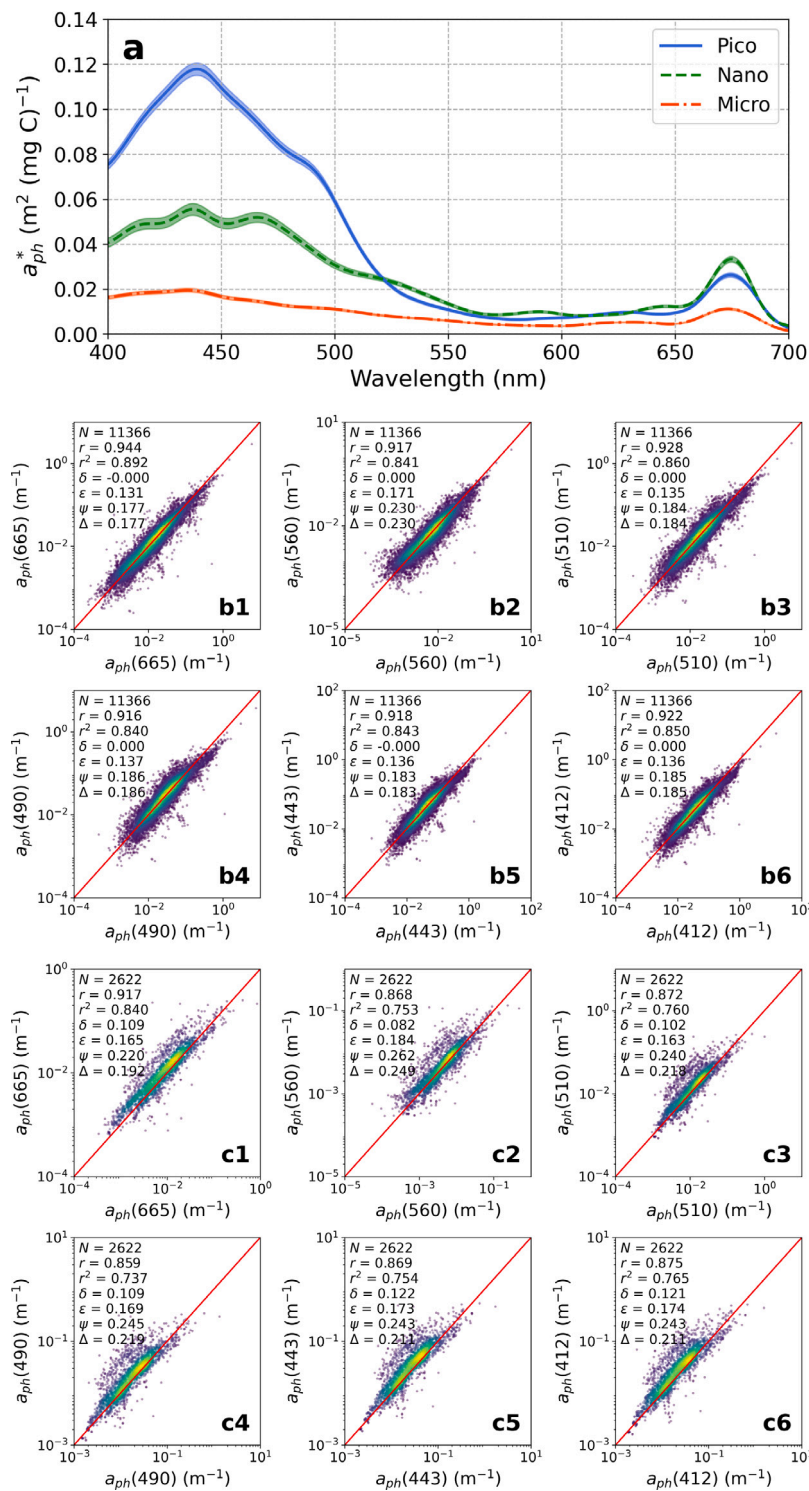
Fig. 3. Chlorophyll-specific absorption coefficients of phytoplankton ($a^*_{ph,i}(\lambda)$, m^2 (mg C)$^{-1}$) retrieved from the a_{ph} model, with shaded areas representing the 5.55 and 94.45% confidence intervals on the distribution (a). Comparison between *in-situ* (x-axis) and modelled (y-axis) $a_{ph}(\lambda)$ at six wavelengths, using the parameterisation dataset (b1–b6) and using the independent validation dataset (c1–c6), respectively. The *p*-values are less than 0.05 for all wavelengths in both datasets. Red line refers to 1:1 line. The model is based on the 16-parameter model (Sun et al., 2023). Results using the 17-parameter model are shown in Supplementary Figure S2. (For interpretation of the references to colour in this figure legend, the reader is referred to the web version of this article.)

et al., 2022). Physical and biological fragmentation of phytoplankton are important sources of NAP in the open ocean, and the size of NAP likely correlates with the dominant size class of phytoplankton in the water. Consequently, the highest slopes are typically associated with the clearest oligotrophic waters, and as turbidity increases, slope values tend to decrease with increasing size, consistent with previous

observations (Bricaud et al., 2010). Note that our pre-processing of all optical datasets (except a_{ph}) excluded samples collected in the highly-turbid coastal waters potentially dominated by larger cell size classes prior to analysis, which may explain the higher S_d in microplankton than nanoplankton. In addition to phytoplankton, factors like zooplankton grazing, bacterial and viral activities also contribute to the NAP

pool. However, the effects of these factors and other processes such as aggregation are not incorporated here. The $a_d^k(\lambda)$ values derived using two SST-dependent models are very similar (see Table S4 in the Supplementary).

The estimated a_d values closely align with parameterisation observations, with all δ being close to zero (Figs. 4b1–b6). Independent validation results (Figs. 4c1–c6) show that the model is reliable, with $r \geq 0.625$ for all five wavelengths with the exception of 665 nm, where the a_d values are typically at a minimum. The inclusion of a_d^k does appear to introduce a slight static cut-off in the lower range for each wavelength. Differences between the validation and parameterisation datasets, especially concerning the content of a_d^k, may account for the overestimation of low a_d values in the independent validation. The contribution of background particles to a_d cannot be neglected (Stramski and Kiefer, 1990; Stramski and Mobley, 1997). However, when accounting for the spatiotemporal variability (Dupouy, 2003), the constant background values used here may overestimate a_d^k in some regions with limited background NAP. The validation results were minimally affected by the two SST-dependent models, with slightly better performance observed when using the 16-parameter model (Fig. 4 and Figure S3 in Supplementary). The proposed a_d model compares favourably with models from previous studies (Bricaud et al., 1998b, 2010), as shown in Section S3.4.2 in Supplementary.

3.2.3. Absorption by CDOM

CDOM absorption, $a_g(\lambda)$, can be modelled as additive sum of Chl-a in each size class (C_i) multiplied by the chlorophyll-specific CDOM absorption coefficient ($a_g^*(\lambda)$) (Brewin et al., 2015a), such that,

$$a_g(\lambda) = \sum_{i=1}^{3} a_{g,i}^*(\lambda) C_i. \tag{13}$$

The spectral shape of $a_g(\lambda)$ typically follows a smooth exponential relationship with wavelength (Bricaud et al., 1981), so that Eq. (13) can be expressed as,

$$a_g(\lambda) = \sum_{i=1}^{3} a_{g,i}^*(\lambda_0) C_i \exp[-S_{g,i}(\lambda - \lambda_0)], \tag{14}$$

where $S_{g,i}$ is the exponential slope for each PSC, and the reference wavelength λ_0 is 440 nm. The $a_{g,i}^*(\lambda_0)$ and $S_{g,i}$ values were derived through minimisation ('lmfit' package in Python) from C_i (calculated from C and SST through Eqs. (2)–(9)) and $\log_{10}$-transformed $a_g(\lambda)$ data.

During the minimisation process, obtaining valid $a_g^*(\lambda_0)$ values for microplankton using both SST-dependent models was challenging, as they were found to be very close to zero. This may be due to the exclusion of samples collected in the coastal waters, which typically have a high proportion of microplankton. More data in the open ocean at high Chl-a concentrations is likely needed to improve the discrimination of spectral characteristics among different size classes. However, it is crucial to include reasonable a_g values for waters dominated by microplankton, given their significant contribution and to maintain consistency with the OCMF structure. To address this issue, we fixed the $a_{g,3}^*(440)$ and $S_{g,3}$, by fitting $a_g^*(440)$ and S_g with the F_3, respectively, and extrapolating to where $F_3 = 1$ (microplankton dominance). The retrieved $a_{g,3}^*(440)$ values are 0.0222 (0.0182–0.0270) and 0.0177 (0.0151–0.0207) for 16- and 17-parameter models, respectively, with the unit of m^2 (mg C)$^{-1}$. The $S_{g,3}$ is 0.155 nm^{-1} for both models, with confidence interval ranging from 0.150 to 0.159 nm^{-1}. The retrieved model parameters are shown in the Table S5 in the Supplementary.

Values of $a_g^*(\lambda_0)$ are higher than $a_d^*(\lambda_0)$ for all the PSCs, with picoplankton having the highest value, followed by nano-, and microplankton. Previous studies have demonstrated that in oceanic waters, CDOM is typically produced by a variety of biological processes, including those involving bacteria, viruses, phytoplankton, and zooplankton (Siegel et al., 2002; Coble, 2007), where phytoplankton growth, grazing, and degradation may all be significant factors in this process (Hu et al., 2006; Organelli and Claustre, 2019). The positive

relationship between $a_g(\lambda)$ and Chl-a (Bricaud et al., 2010), as shown in Section S3.4.3 in the Supplementary, along with the relationship between size structure and Chl-a, may explain the variations of $a_g^*(\lambda_0)$ in different size classes here. Similarly, the S_g values are on average higher than the S_d values. The range of the size-specific S_g retrieved in this study was broader than previous findings while remaining consistent with them (Babin et al., 2003; Organelli et al., 2014), possibly due to the large *in-situ* dataset used here. The S_g has been proposed as an indicator of the CDOM composition driven by photobleaching or production (Nelson and Siegel, 2013). Variations in S_g values are primarily due to the process of photobleaching in surface oceanic waters (Twardowski and Donaghay, 2002), which are typically less affected by riverine inputs, have higher solar radiation and increased stratification, and tend to be dominated by smaller size classes (Bricaud et al., 2012).

Compared to a_{ph} and a_d, the a_g data points show greater dispersion, resulting in relatively weak correlations between *in-situ* and modelled values using the parameterisation dataset (Figs. 5b1–b6). As for the independent validation in Figs. 5c1–c6, there is good agreement between model estimates and observations, with r above 0.629 at short wavelengths (≤ 510 nm). While at longer wavelengths, the model manages to represent the overall trends in a_g with relatively similar δ, despite the scattered nature of the data points. The scatter can be attributed to very low values in the *in-situ* observations at longer wavelengths, resulting from a reduced signal-to-noise ratio and increased measurement uncertainty. This is due to the nature of CDOM, such as its weak signal, variability in composition, and temporal variations in sources and sinks (Nelson et al., 1998), making a_g a difficult IOP to measure. The two SST-dependent models show little influence on the retrieval results and the validation results, with slightly better performance observed when using the 16-parameter model (Fig. 5 and Figure S4 in Supplementary). The proposed a_g model was compared with models from previous studies (Morel, 2009; Bricaud et al., 2010; Dall'Olmo et al., 2017), as shown in Section S3.4.3 in the Supplementary.

3.2.4. Total absorption

With the development of models for all particulate and dissolved absorbing components, the total absorption coefficients, $a(\lambda)$, can be expressed as the additive sum of these constituents and water (Prieur and Sathyendranath, 1981), such that,

$$a(\lambda) = a_w(\lambda) + a_{ph}(\lambda) + a_d(\lambda) + a_g(\lambda), \tag{15}$$

where $a_{ph}(\lambda)$, $a_d(\lambda)$, and $a_g(\lambda)$ were described in the sections above. The absorption coefficient of pure water, $a_w(\lambda)$, is obtained from Lee et al. (2015), where values below 550 nm are derived from R_{rs} measurements in oligotrophic oceans, and values beyond 550 nm are adopted from Pope and Fry (1997). The effect of temperature on $a_w(\lambda)$ was not considered in this study, since Wei et al. (2021) suggested that the temperature has a negligible effect on $a_w(\lambda)$ within the range of 19–27 °C, which covers the most oligotrophic waters where a_w tends to have a more significant effect on the R_{rs}.

3.3. Backscattering

The backscattering coefficient is contributed by particulate constituents and water molecules. Similar to absorption, the particulate component, excluding the NAP background, can be represented as the product of its chlorophyll-specific backscattering spectrum and Chl-a concentration. In the OCMF, we start by modelling the particle backscattering that can be measured directly from the ocean. Then, we split the particle backscattering into contributions from phytoplankton and NAP.

3.3.1. Backscattering by particles

Following Brewin et al. (2012), particle backscattering, $b_{bp}(\lambda)$, can be modelled as an additive sum of the Chl-a in each PSC (C_i) multiplied
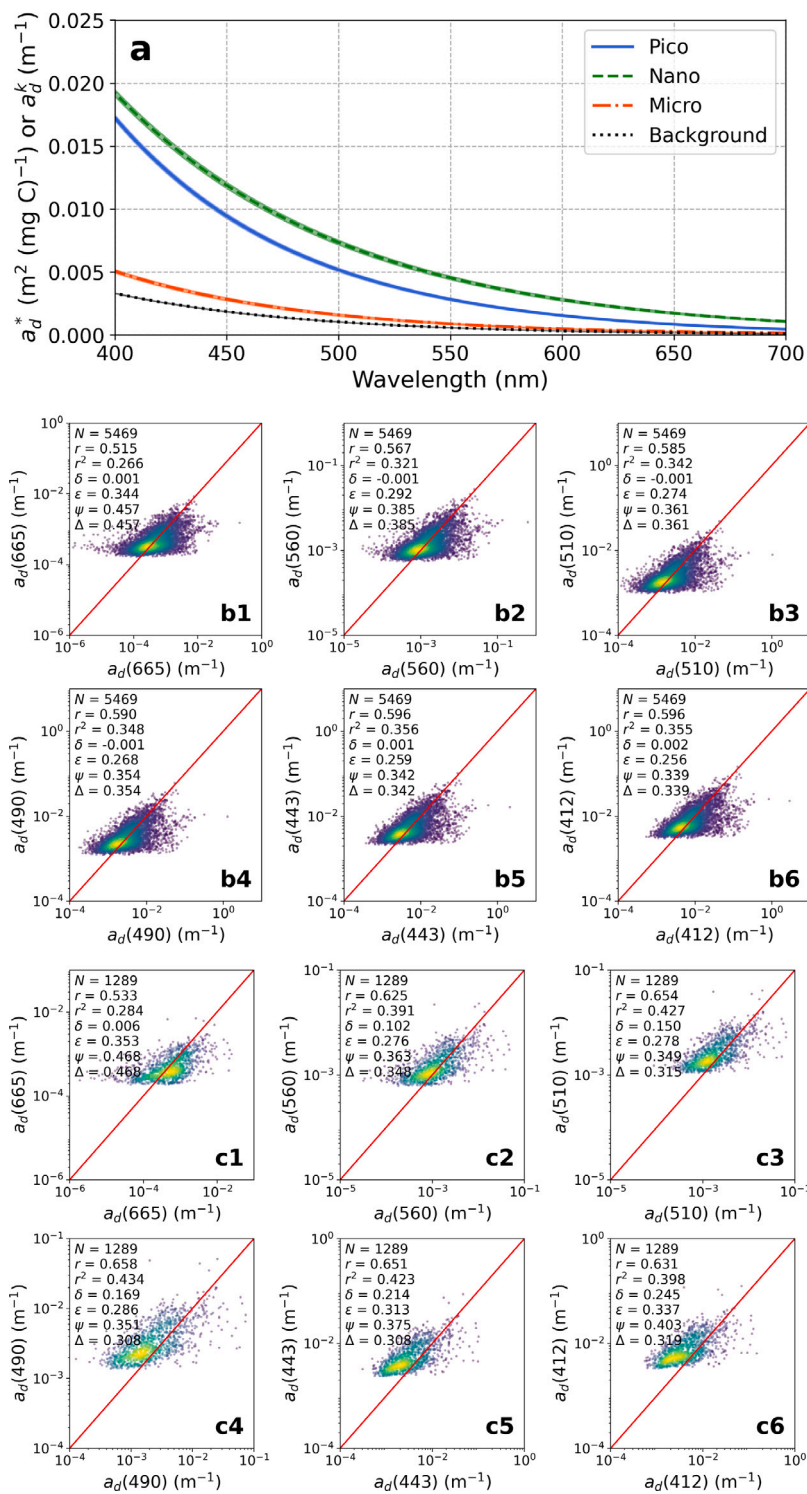
Fig. 4. Chlorophyll-specific absorption coefficients of NAP ($a_{d,i}^*(\lambda)$, m^2 (mg C)$^{-1}$) and the absorption coefficient of background ($a_d^k(\lambda)$, m^{-1}), retrieved from the a_d model, with shaded areas representing the 5.55 and 94.45% confidence intervals on the distribution (a). Note that the shaded areas may appear less pronounced due to the narrow range of the confidence intervals. Comparison between *in-situ* (x-axis) and modelled (y-axis) $a_d(\lambda)$ at six wavelengths, using the parameterisation dataset (b1–b6) and using the independent validation dataset (c1–c6), respectively. The *p*-values are less than 0.05 for all wavelengths in both datasets. Red line refers to 1:1 line. The model is based on the 16-parameter model (Sun et al., 2023). Results using the 17-parameter model are shown in Supplementary Figure S3. (For interpretation of the references to colour in this figure legend, the reader is referred to the web version of this article.)
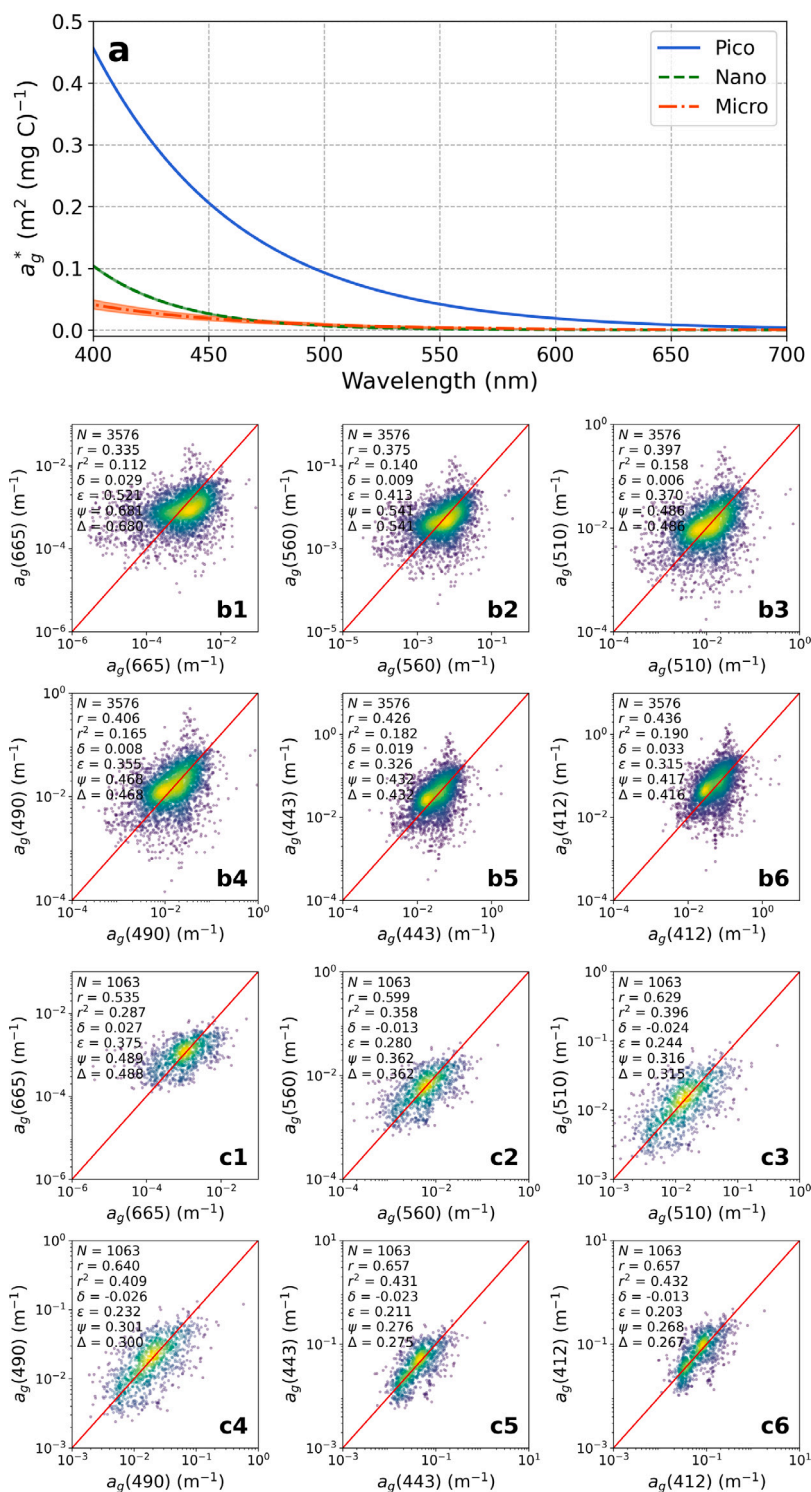
Fig. 5. Chlorophyll-specific absorption coefficients of CDOM ($a_{g,i}^*(\lambda)$, m^2 (mg C)$^{-1}$) retrieved from the a_g model, with shaded areas representing the 5.55 and 94.45% confidence intervals on the distribution (a). Note that the shaded areas may appear less pronounced due to the narrow range of the confidence intervals. Comparison between *in-situ* (x-axis) and modelled (y-axis) $a_g(\lambda)$ at six wavelengths, using the parameterisation dataset (b1–b6) and using the independent validation dataset (c1–c6), respectively. The *p*-values are less than 0.05 for all wavelengths in both datasets. Red line refers to 1:1 line. The model is based on the 16-parameter model (Sun et al., 2023). Results using the 17-parameter model are shown in Supplementary Figure S4. (For interpretation of the references to colour in this figure legend, the reader is referred to the web version of this article.)

by the chlorophyll-specific backscattering coefficient of particles ($b^*_{bp,i}$), and a constant background (b^k_{bp}, akin to $a^k_d(\lambda)$ in absorption), mainly associated with a background of NAP (Bellacicco et al., 2019; Kheireddine et al., 2021),

$$b_{bp}(\lambda) = \sum_{i=1}^{3} b^*_{bp,i}(\lambda) C_i + b^k_{bp}(\lambda). \tag{16}$$

Assuming that $b_{bp}(\lambda)$ can be expressed as a power-law function of wavelength (Lee et al., 2002), Eq. (16) can be formulated as follows:

$$b_{bp}(\lambda) = \sum_{i=1}^{3} b^*_{bp,i}(\lambda_0)(\lambda/\lambda_0)^{-\gamma_i} C_i + b^k_{bp}(\lambda), \tag{17}$$

where γ_i determines the spectral shape of the backscattering, and λ_0 is the reference wavelength at 550 nm. When the $b^k_{bp}(\lambda)$ was also expressed as a power function (i.e., $b^k_{bp}(\lambda_0)(\lambda/\lambda_0)^{-\gamma_k}$) and parameters for both phytoplankton and the background were retrieved simultaneously, obtaining stable retrieval results during the minimisation process became challenging. Therefore, to simplify the equation and obtain realistic results, the $b^k_{bp}(\lambda)$ for each wavelength was fixed by computing the 5th percentile of the *in-situ* $b_{bp}(\lambda)$ values from ultra-oligotrophic waters (i.e., Chl-a < 0.04 mg m^{-3}, Alvain et al., 2008; Leonelli et al., 2022). The remaining backscattering coefficients, $b_{bp}(\lambda)$ - $b^k_{bp}(\lambda)$, were then used for deriving $b^*_{bp,i}(\lambda_0)$ and γ_i in each size class, through minimisation ('lmfit' package in Python). The inputs of Eq. (17) were C_i (calculated from C and SST through Eqs. (2)–(9)) and $\log_{10}$-transformed $b_{bp}(\lambda)$.

Similar to the results found in CDOM absorption (Section 3.2.3), $b^*_{bp}(\lambda_0)$ values for microplankton approached zero in the initial minimisation process. To include valid b_{bp} values for waters dominated by microplankton and maintain alignment with the OCMF, the $b^*_{bp,3}(550)$ was fixed, by fitting $b^*_{bp}(550)$ (with $b^k_{bp}(550)$ removed) with the F_3, and extrapolating to where $F_3 = 1$ (microplankton dominance). The retrieved $b^*_{bp,3}(550)$ values are 0.0022 (0.0021–0.0022) and 0.0021 (0.0021–0.0022) (m^2 (mg C)$^{-1}$) for 16- and 17-parameter models, respectively. Since a previous study found the γ_3 value not statistically different from zero for microplankton-dominated waters (Brewin et al., 2012), it was fixed at 0. Table S6 in the Supplementary shows the parameters used in Eq. (17).

Fig. 6a shows the retrieved results of $b^*_{bp}(\lambda)$ and $b^k_{bp}(\lambda)$. In general, the water dominated by nanoplankton and their covarying particles has the highest specific backscattering value over the entire spectrum. It is followed by picoplankton-dominated water, with relatively little difference between the two size classes. The lowest values were observed in water dominated by microplankton, where the values were fixed. The $b^*_{bp}(550)$ retrieved in this study for pico- and nanoplankton align with established observations (Brewin et al., 2012; Martinez-Vicente et al., 2012), and lower values for larger cells are in agreement with previous studies (Dall'Olmo et al., 2012; Barbieux et al., 2018; Soja-Woźniak et al., 2020). As for the slope, pico- and nanoplankton show similar γ values that are statistically different from zero, consistent with expectation that a steeper power exponent is likely to be associated with low Chl-a water that is dominated by small particles (Loisel et al., 2006; Kostadinov et al., 2009; Reynolds and Stramski, 2019). The $b^k_{bp}(\lambda)$ values obtained in this study are within the range observed in the global ocean (Bellacicco et al., 2019). However, they show a modest difference from those reported in other oceanic regions (Behrenfeld et al., 2005; Brewin et al., 2012; Kheireddine et al., 2021), suggesting that $b^k_{bp}(\lambda)$ has spatiotemporal variability (Bellacicco et al., 2019).

With the exception of a few outliers within a large dataset, the b_{bp} model performs well when compared with the observations from both the parameterisation and validation datasets (Figs. 6b1–b6 and 6c1–c6), with comparable statistics. When compared to *in-situ* values at all six wavelengths, independent validation shows that the model provides satisfactory estimation of b_{bp}, with r over 0.593 and low differences (ψ < 0.225). The model slightly underestimates b_{bp} at larger

values, as indicated by a negative bias. Both SST-dependent models had minimal impact on the retrieval results and validation results, with a slight improvement observed when using the 17-parameter model (Fig. 6 and Figure S5 in Supplementary). The proposed b_{bp} model compares favourably with models from previous studies (Huot et al., 2008; Dall'Olmo et al., 2009; Brewin et al., 2012), as shown in Section S3.4.4 in the Supplementary.

3.3.2. Backscattering by phytoplankton and NAP

Particulate backscattering is composed of both phytoplankton and NAP (e.g., detritus), referred to as $b_{bph}(\lambda)$ and $b_{bd}(\lambda)$, respectively (Fig. 2). In this study, we extended the particulate backscattering model (Section 3.3.1) to distinguish between the algal and non-algal contributions. The $b_{bph}(\lambda)$ can be expressed as an additive sum of the Chl-a in each PSC (C_i) multiplied by its corresponding chlorophyll-specific backscattering coefficient of phytoplankton ($b^*_{bph,i}(\lambda)$), such that,

$$b_{bph}(\lambda) = \sum_{i=1}^{3} b^*_{bph,i}(\lambda_0)(\lambda/\lambda_0)^{-\gamma_{ph,i}} C_i, \tag{18}$$

where $\gamma_{ph,i}$ is the power coefficient of the phytoplankton backscattering, and λ_0 is the reference wavelength at 550 nm. In Eq. (18), the input $b_{bph}(\lambda)$ on the left was calculated using a 1% quantile regression under the assumption that 1% of the $b_{bp}(\lambda)$-$b^k_{bp}(\lambda)$ is contributed by phytoplankton, which is akin to estimating phytoplankton carbon contributions to particulate organic carbon at different Chl-a concentrations (Sathyendranath et al., 2009), as well as estimating phytoplankton carbon and nitrogen from Chl-a (Maniaci et al., 2022). The fitted 1% quantile data was then used to retrieve parameters in Eq. (18). Similar to $b^*_{bp}(\lambda_0)$, the $b^*_{bph}(\lambda_0)$ values for microplankton approached zero during the minimisation process. Therefore, the $b^*_{bph,3}(550)$ was fixed at 0.0002 m^2 (mg C)$^{-1}$, taken from backscattering measurements of uni-algal cultures, e.g., *Prorocentrum micans* (Table 1 in Ahn et al., 1992) and *Ditylum brightwellii* (Figure 5C in Whitmire et al., 2010). The $\gamma_{ph,3}$ was set to zero. Consequently, the $b^*_{bd}(\lambda)$ for three size classes were calculated through subtracting $b^*_{bph}(\lambda)$ from $b^*_{bp}(\lambda)$. Since the $b_{bd}(\lambda)$ can also be written as an additive sum of the chlorophyll-specific NAP backscattering coefficient ($b^*_{bd,i}(\lambda)$) multiplied by its corresponding Chl-a (C_i), it can be expressed as

$$b_{bd}(\lambda) = \sum_{i=1}^{3} b^*_{bd,i}(\lambda_0)(\lambda/\lambda_0)^{-\gamma_{d,i}} C_i + b^k_{bp}(\lambda), \tag{19}$$

the $b^*_{bd}(\lambda_0)$ and $\gamma_{d,i}$ can be retrieved from fitting the $b^*_{bd}(\lambda)$ to the power-law function. The parameters used in the Eqs. (18) and (19) are listed in the Table S7 in the Supplementary.

Fig. 7a indicates that phytoplankton size could affect $b^*_{bph}(\lambda)$, with picoplankton having the highest value, followed by nano- and microplankton. Note that in this study, the $b_{bp}(\lambda)$ are the fitting results obtained from the power-law function of the multispectral b_{bp} measurements, with the corresponding 1% quantile fraction being $b_{bph}(\lambda)$. Therefore, finer backscattering spectral features of phytoplankton (Whitmire et al., 2010) are not considered here. Because of the 1% quantile assumption for the $b_{bph}(\lambda)$ established earlier, specific backscattering of NAP are often higher than those of phytoplankton for all three size classes (Fig. 7b). Nonetheless, the sources of backscattering and its variability remain controversial (Stramski et al., 2001; Dall'Olmo et al., 2009; Organelli et al., 2018). Further investigations are required on the 1% assumption to determine whether an alternative percentage should be considered. The higher $b^*_{bp}(\lambda)$ and $b^*_{bd}(\lambda)$ in nanoplankton-dominated waters might result from the enhanced backscattering of inorganic particles per unit Chl-a, which calcifying phytoplankton like coccolithophores may be responsible for (Balch et al., 1991; Terrats et al., 2020), a common nanoplankton species worldwide. Slopes of phytoplankton backscattering, $\gamma_{ph,i}$, are in general higher than those of total particles (γ_i) and NAP ($\gamma_{d,i}$), suggesting that NAP sizes may be larger than phytoplankton for each class (Slade
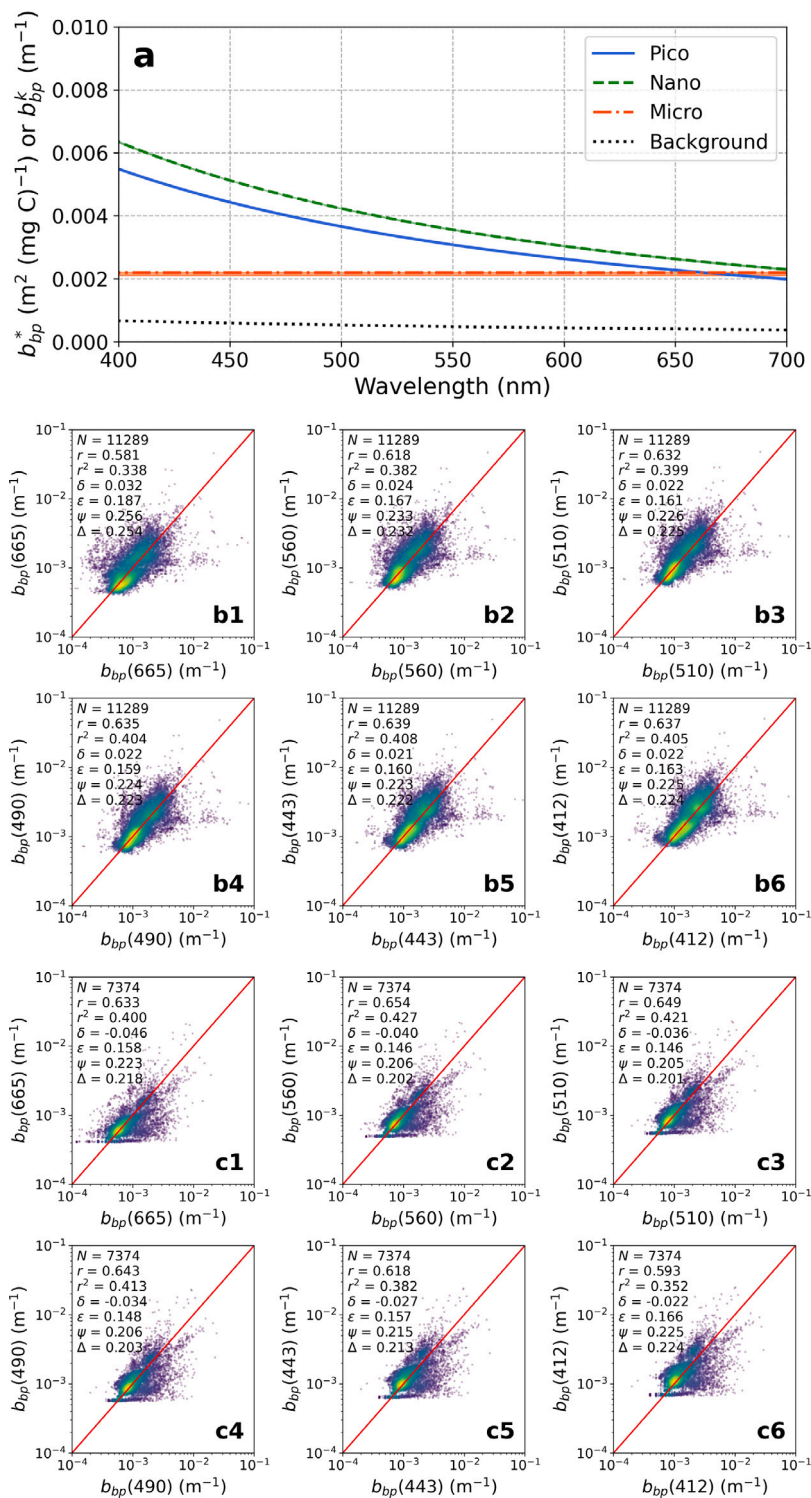
Fig. 6. Chlorophyll-specific backscattering coefficients of particles ($b_{bp,i}^*(\lambda)$, m^2 (mg C)$^{-1}$) and the backscattering coefficient of background ($b_{bp}^k(\lambda)$, m^{-1}), retrieved from the b_{bp} model, with shaded areas representing the 5.55 and 94.45% confidence intervals on the distribution (a). Note that the shaded areas may appear less pronounced due to the narrow range of the confidence intervals. Comparison between *in-situ* (x-axis) and modelled (y-axis) $b_{bp}(\lambda)$ at six wavelengths, using the parameterisation dataset (b1–b6) and using the independent validation dataset (c1–c6), respectively. The *p*-values are less than 0.05 for all wavelengths in both datasets. Red line refers to 1:1 line. The model is based on the 16-parameter model (Sun et al., 2023). Results using the 17-parameter model are shown in Supplementary Figure S5. (For interpretation of the references to colour in this figure legend, the reader is referred to the web version of this article.)
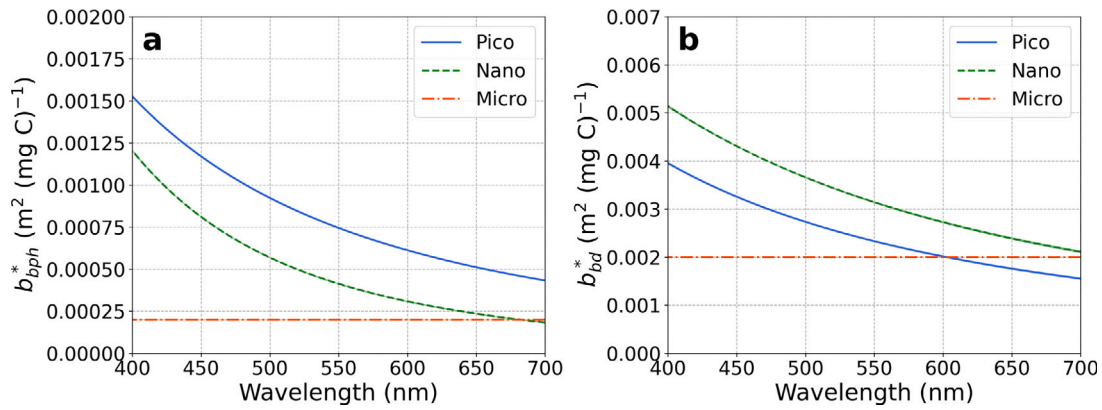
Fig. 7. Chlorophyll-specific backscattering coefficients of phytoplankton ($b^*_{bph,i}(\lambda)$, m^2 (mg C)$^{-1}$) retrieved from the 1% quantile of the b_{bp}-b^k_{bp} (a). Chlorophyll-specific backscattering coefficients of NAP ($b^*_{bd,i}(\lambda)$, m^2 (mg C)$^{-1}$) retrieved from subtraction of $b^*_{bph}(\lambda)$ from $b^*_{bp}(\lambda)$ (b). The shaded areas represent the 5.55 and 94.45% confidence intervals on the distribution. Note that the shaded areas may appear less pronounced due to the narrow range of the confidence intervals. The model is based on the 16-parameter model (Sun et al., 2023). Results using the 17-parameter model are shown in Supplementary Figure S6. (For interpretation of the references to colour in this figure legend, the reader is referred to the web version of this article.)

and Boss, 2015), possibly due to particle aggregation (Stemmann and Boss, 2012). It is essential to acknowledge that the natural ocean contains diverse water constituents with varying backscattering properties (Stramski et al., 2004), whereas this study focuses on a limited set, including phytoplankton and NAP. Therefore, the chlorophyll-specific backscattering for each constituent and the spectral slope are intended to capture broad distinctions in size classes, and may require further refinement in the future.

3.3.3. Total backscattering

The total backscattering coefficients, $b_b(\lambda)$, can be expressed as the additive sum of backscattering coefficients of pure water ($b_{bw}(\lambda)$) and those particles mentioned above, such that,

$$b_b(\lambda) = b_{bw}(\lambda) + b_{bp}(\lambda), \tag{20}$$

or

$$b_b(\lambda) = b_{bw}(\lambda) + b_{bph}(\lambda) + b_{bd}(\lambda). \tag{21}$$

The $b_{bw}(\lambda)$ used in this study was calculated following previous studies (Zhang and Hu, 2009; Zhang et al., 2009), which changes with temperature and salinity. In this study, the temperature used in the $b_{bw}(\lambda)$ was obtained from the matched daily OISST data (see Section 2.3.1) and the salinity was kept at 35 ppt.

3.4. Remote sensing reflectance

Using a forward model that explicitly considers the particle and molecule scattering phase-function effects (Lee et al., 2013), the remote sensing reflectance (not accounting for Raman scattering), $R_{rs}(\lambda)$, can be estimated from the total absorption and total backscattering coefficients (Sections 3.2 and 3.3), such that,

$$R_{rs}(\lambda, \Omega) = (G^w_0(\Omega) + G^w_1(\Omega) \frac{b_{bw}(\lambda)}{\kappa(\lambda)}) \frac{b_{bw}(\lambda)}{\kappa(\lambda)}$$
$$+ (G^p_0(\Omega) + G^p_1(\Omega) \frac{b_{bp}(\lambda)}{\kappa(\lambda)}) \frac{b_{bp}(\lambda)}{\kappa(\lambda)}, \tag{22}$$

where Ω represents the sun-sensor angular geometry for R_{rs}, including solar zenith angle, sensor nadir-view angle, and sensor azimuth angle in relation to the solar plane, and $\kappa(\lambda) = b_b(\lambda) + a(\lambda)$. For nadir-viewed R_{rs}, $G^w_0(\Omega)$, $G^w_1(\Omega)$, $G^p_0(\Omega)$, and $G^p_1(\Omega)$ are 0.0604, 0.0406, 0.0402, 0.1310 sr^{-1}, respectively (Lee et al., 2011).

4. Results and discussion

4.1. Initial model assessment and CDOM absorption adjustment

With all the chlorophyll-specific IOPs derived, the $R_{rs}(\lambda)$ can be calculated using the OCMF (Eq. (22)) with the input of Chl-a and SST. The *in-situ* independent R_{rs} dataset collected after 2016 was used to validate the accuracy of the OCMF. The green dashed line in Fig. 8 shows that the modelled $R_{rs}(\lambda)$ were underestimated at blue and green wavelengths with notable negative biases, compared to the *in-situ* measurements. Through individual assessments of the chlorophyll-specific IOPs with previous models (Section S3.4 in Supplementary), we attributed these biases to an overestimation of $a_g(\lambda)$. As shown in Figure S15 in the Supplementary, the $a_g(443)$ estimated from our model is the highest compared with two previous models of a_g (Morel, 2009; Dall'Olmo et al., 2017). Previous studies have highlighted that a_g can have a significant effect on R_{rs} at blue wavelengths, especially at the lower Chl-a range where the blue signal is highest (Morel and Gentili, 2009; Naik et al., 2013; Huot and Antoine, 2016). Therefore, an adjustment of a^*_g parameters was performed using the *in-situ* training R_{rs} dataset collected prior to 2016 ($N = 2668$), to improve radiometric closure between R_{rs} and IOPs. Parameter values for a_w, a_{ph}, a_d, b_{bw}, and b_{bp} were sourced from the developed OCMF, while we linearly scaled the three $a^*_g(440)$ parameters (same scaling factor for each PSC), leaving the three S_g values unchanged (i.e., those derived from Eq. (14)). The scaling factors were obtained for 16- and 17-parameter models separately through minimisation ('lmfit' package in Python) on R_{rs}. The resulting scaling factors are 0.44 (± 0.001) and 0.45 (± 0.001), respectively, suggesting that the initial values of a^*_g were overestimated by more than twice. The adjusted a^*_g parameters results in better agreement with the two previous models (Figure S15 in the Supplementary). Interestingly, in both these studies, the models were either parameterised using similar closure experiments (Morel, 2009), or parameterised using a new technique to measure a_g (Dall'Olmo et al., 2017), rather than the traditional methods used in our compiled dataset. Our proposed a_g adjustment may require refining as more data become available, and better techniques for measuring a_g emerge.

The adjustment of a_g is found to significantly improve the accuracy of the OCMF in estimating the R_{rs}, but a slight underestimation remains (red line in Fig. 8). These uncertainties may be related to systematic differences in the R_{rs} datasets pre- and post-2016, or may arise from proposed IOP models of other water constituents. For example, the
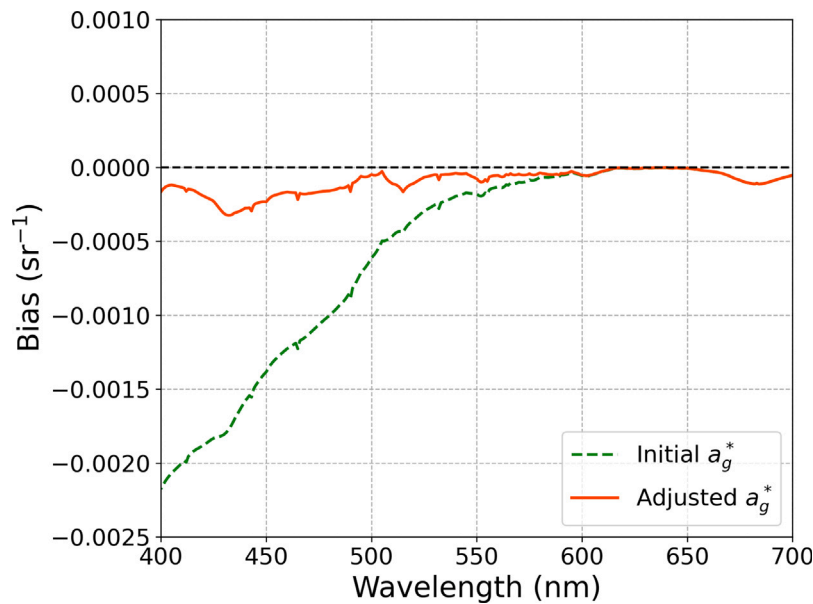
Fig. 8. The bias between *in-situ* measured and modelled $R_{rs}(\lambda)$ using the OCMF at all wavelengths, using the independent validation dataset ($N = 579$). The red solid and green dashed lines represent the results using the initial and adjusted a_g^*, respectively. Note that here the bias was computed in linear space, with the unit of sr^{-1}. The model is based on the 16-parameter model (Sun et al., 2023). Results using the 17-parameter model are shown in Supplementary Figure S7. (For interpretation of the references to colour in this figure legend, the reader is referred to the web version of this article.)

overestimation of a_d (Fig. 4) and the underestimation of b_{bp} (Fig. 6) at short wavelengths could also lead to the underestimation of R_{rs}. The $a_w(\lambda)$ in Lee et al. (2015) has been refined for shorter wavelengths to achieve a better closure of R_{rs}–IOPs (Yu et al., 2019). However, its dependency on temperature and salinity was not considered in the OCMF (Röttgers et al., 2014). The $b_{bw}(\lambda)$, modelled as functions of temperature and salinity, has shown excellent precision (Zhang et al., 2009); however, salinity was set to 35 ppt in this study for model simplification. The IOPs of pure water need refinement to further reduce uncertainties (Werdell et al., 2018). It is crucial to account for Raman scattering because of its importance in clear oceans (Sathyendranath and Platt, 1998; Westberry et al., 2013). Despite not being included directly in our proposed forward model, the Raman scattering was removed (Lee et al., 2013) from the *in-situ* R_{rs} in these comparisons. Other sources of inelastic scattering are not considered here either, such as the fluorescence caused by the Chl-a and CDOM (Lee et al., 1994; Li et al., 2016), but could be included in the future. Moreover, complete details regarding the collection of *in-situ* R_{rs} datasets from various sources were not always available. As a result, the BRDF (bidirectional reflectance distribution function) correction (Morel et al., 2002; Lee et al., 2011) was not considered here, and the measured R_{rs} might be higher than the modelled, simply due to differences in angular light conditions.

In addition to uncertainties in model parameters and in the forward modelling framework, biases between modelled and measured R_{rs} can arise from the quality of the *in-situ* measurements (Tonizzo et al., 2016). Despite our extensive efforts to gather data from aquatic environments globally, variability in instrumentation, spectral resolutions, processing approaches and correction methods all introduce uncertainty into the modelling process (Valente et al., 2022). This variability is further amplified by the environmental variability that characterise each sample, such as those in the R_{rs} dataset (Rudorff et al., 2014). Furthermore, the compiled b_{bp} dataset include four types of Chl-a measurements (i.e., HPLC, line-height, *in-vitro* fluorometric, or *in-vivo* fluorescence methods), each of which contain varying levels of uncertainty (Roesler et al., 2017). The independent collection of each optical dataset within this study leads to mismatches between in-situ IOPs and R_{rs} measurements across time and space, which may introduce additional

uncertainties. This makes full closure assessments (e.g., total absorption and total backscattering) and temporal variability assessments challenging. These limitations highlight the need for high quality optical matching datasets for accurate closure interpretation (Pitarch et al., 2016).

4.2. Forward model validation and comparison

Using *in-situ* Chl-a and the matched SST, alongside all the derived parameters of the OCMF after CDOM adjustment (Tables S2–S7), the R_{rs} were calculated for all wavelengths and compared with the independent *in-situ* R_{rs} validation dataset (post 2016, $N = 579$), to evaluate the OCMF performance. Overall, the OCMF is seen to perform reasonably well in estimating R_{rs} (Fig. 9). Statistical tests indicate that the best agreements in magnitude are observed at wavelengths 412 and 443 nm, with r surpassing 0.697 and ψ values of 0.00149 and 0.00129 sr^{-1}, respectively, followed by 560 and 665 nm, where r exceeds 0.559 and ψ are 0.00053 and 0.00015 sr^{-1}, respectively (Figs. 9a1–a6). However, the model captures less of the variability in *in-situ* R_{rs} at 490 and 510 nm, with lower r^2 values. This may be due to the a_{ph} model performing less accurately at these wavelengths (Fig. 3), where variability can increase depending on the composition of phytoplankton present and their accessory pigment structure (Bricaud et al., 2004). Additionally, the variability in a_g for green wavelengths is high (Fig. 5), and the overestimation of a_d values when Chl-a is low (Fig. 4) could also contribute to higher uncertainty at these wavelengths. The biases (δ) indicate that the OCMF has a slight tendency to underestimate R_{rs} at all six wavelengths, with the largest bias of -0.00030 sr^{-1} observed at 443 nm, although the closeness between RMSD and centre-patterned RMSD indicates this systematic difference is small compared to random differences between the model and the data. To evaluate further the sensitivity of the OCMF, we conducted Monte Carlo (bootstrap) simulations, and used the independent validation dataset to test the sensitivity of the validation metrics to uncertainty in model parameters (Tables S2–S7 in the Supplementary). One thousand simulations were performed, and for each iteration, model parameters were randomly assigned values within their confidence intervals, and statistical tests were calculated for each iteration. The mean and standard deviation

of the 1000 iterations were then determined. Results showed that the statistical tests of the R_{rs} validation with randomly selected model parameters were close to the results in Fig. 9 (not shown), demonstrating these validation metrics were not sensitive to uncertainties in model parameters. The band ratios of R_{rs} were also validated, given that many biogeochemical properties depend on the shape of R_{rs} (O'Reilly et al., 1998; Stramski et al., 2008b; Blondeau-Patissier et al., 2014). The modelled R_{rs} shape, normalised at 560 nm, agreed well with the shape of the *in-situ* R_{rs}, with r over 0.862 at four wavelengths except 665 nm and low ψ values across most wavelengths (Figs. 9b1–b6). Differences between the two SST-dependent phytoplankton size structure models on the validation results of R_{rs} were found to be negligible (Fig. 9 and Figure S8 in the Supplementary).

To further assess the proposed OCMF, particularly the impact of incorporating the effect of temperature on the ocean-colour, we use a Case-1 model assembled from a previous study for comparison (Model J in Brewin et al. (2015b), see their Section 3.1.10). Model J is a forward model in which all the IOP models and R_{rs} model used differ from our proposed OCMF. This model was deemed suitable, given it performed well in an inter-comparison study (Brewin et al., 2015b). Owing to the small size of the independent validation R_{rs} ($N = 579$), we were restricted to further subdivide it for temperature related assessments. Therefore, we used an extra published global dataset from Graban et al. (2020) that is independent of our dataset (see Section 2.3.3). Note that in this dataset, rather than *in-situ* radiometric measurements, the corresponding R_{rs} of *in-situ* Chl-a measurements are from OC-CCI satellite data. Furthermore, both pre and post 2016 samples from the dataset were used, resulting in a larger number of samples with broader ranges of Chl-a and temperature.

Using the whole Graban et al. (2020) dataset ($N = 9050$), the OCMF shows higher accuracy, with biases closer to zero at all six wavelengths, where there is significant underestimation of the Model J from Brewin et al. (2015b), regarding both magnitude and shape of the R_{rs} (Figs. 10a1 and 10b1). The underestimation of R_{rs} using the OCMF at the blue wavelengths aligns with the independent validation result (Fig. 9). To assess the performance of the OCMF across different temperature ranges, the whole Graban et al. (2020) dataset was evenly partitioned into five sub-datasets based on temperature, encompassing low (−0.61 to 15.07 °C), low-medium (15.10 to 20.34 °C), medium (20.38 to 24.10 °C), medium-high (24.12 to 26.48 °C), and high (26.49 to 30.82 °C) ranges. The biases were then compared within each temperature range (Figs. 10a2–a6 and 10b2–b6). Results indicate that the OCMF has biases consistently closer to zero under varying temperature conditions, effectively highlighting that incorporating size structure and temperature into the OCMF significantly improves the accuracy in modelled R_{rs} compared to the Model J from Brewin et al. (2015b). There are exceptions for a few wavelengths in the low-temperature waters (Figs. 10a2 and 10b2), where the temperature range is wider than other sub-datasets. In these cases, Model J shows a smaller bias. This overestimation might result from the limited availability of data in low-temperature water available for model parameterisation (Supplementary Figures S1-1–S1-5). Additionally, the small quantity of low-temperature waters in Graban et al. (2020) dataset may also contribute to these differences (Supplementary Figure S1-6). It will be important to further refine and validate the proposed OCMF as more samples in low-temperature waters become available. The comparison of bias between the two models has valuable implications for studying the impact of changing environmental conditions, such as those driven by temperature-affected climate change, on ocean colour. Similar comparison results were also obtained when using the 17-parameter model (Figure S9 in Supplementary).

The IOP models used in Model J from Brewin et al. (2015b) were compared with those proposed in this study, which showed comparable but slightly lower accuracy, based on *in-situ* datasets (details in the Section S3.4 in Supplementary). Besides, differences in the sources of

a_w, b_{bw}, and the R_{rs} model used between the OCMF and Model J may also be responsible for the variations in the accuracy of the modelled R_{rs}. To evaluate the impact of these differences, a stepwise replacement of each component in Model J with its counterpart from the OCMF model was performed by comparing the biases, similar to Figs. 10a1 and 10b1, using the whole (Graban et al., 2020) dataset (not shown). Regarding the R_{rs} magnitude, substituting the b_{bp} model resulted in a modest reduction of the underestimation observed in the original Model J, followed by the substitutions of the a_w, R_{rs}, a_{ph}, and a_g models with limited improvements. As for the shape of R_{rs}, applying the a_w model from Lee et al. (2015) resulted in notable reductions in underestimation. This substitution improved the closure of R_{rs}–IOPs, especially in the blue wavelength range, and brought the bias closer to the OCMF proposed in this study. Furthermore, replacing the a_{ph}, a_g, R_{rs}, and b_{bw} models, as proposed in this study, also contributed to accuracy improvements, although relatively small.

4.3. Impacts of temperature on size structure and resulting effects on remote sensing reflectance

Fig. 11 shows the maximum band ratio of R_{rs} estimated using the proposed OCMF with the inputs of simulated Chl-a and SST. The regionally-tuned OC3 algorithms for the Southern Ocean (Johnson et al., 2013; Pereira and Garcia, 2018) and globally-tuned OC3 algorithm (O'Reilly and Werdell, 2019) are overlaid for comparison. All these algorithms are applied using MODIS (Moderate Resolution Imaging Spectro-radiometer) wavelengths.

The maximum band ratio shows relatively small variations for higher Chl-a ranges (>1 mg m^{-3}), whereas lower Chl-a ranges show more pronounced variations (Fig. 11a). As SST decreases for the same Chl-a concentration, the dominant size classes of phytoplankton shift from smaller cells to larger cells (Figs. 11b–d), leading to a significant increase in blue-to-green ratio. These findings are in agreement with a early regional work in the North Atlantic Ocean, which used an ocean-colour model integrated with an SST-dependent phytoplankton group absorption (Brewin et al., 2019). The globally-tuned OC3 algorithm (O'Reilly and Werdell, 2019) agrees well with the proposed model estimates in warmer water conditions, especially in regions with low Chl-a concentration. This agreement could be due to the dataset distribution employed in calibrating the OC3 algorithm, given that subtropical regions are typically associated with warm and low-chlorophyll waters.

Remarkably, the maximum band ratio simulations are consistent with findings from the regional studies in cold waters (e.g., Southern Ocean, Johnson et al., 2013; Pereira and Garcia, 2018). Their regionally-tuned OC3 algorithms produced higher maximum band ratios for a given Chl-a, which may be due to a higher fraction of large-celled phytoplankton typically found in colder waters. These results align with previous findings, showing that the Southern Ocean has distinct bio-optical properties (Arrigo et al., 1998; Ferreira et al., 2018; Robinson et al., 2021), for example, high blue–green reflectance ratios, low backscattering, and low chlorophyll-specific absorption. These evidences back up the higher contribution of large celled phytoplankton in the area and suggest that standard ocean-colour algorithms are unsuitable for this region. For example, a study showed that Chl-a tends to be underestimated by about 50% (Szeto et al., 2011), possibly due to different phytoplankton size composition (and pigment composition) and different amounts of non-algal substances (Clementson et al., 2001; Reynolds et al., 2001). These differences are explicitly considered in our OCMF.

However, there are some differences in the maximum band ratio between the proposed OCMF and other regionally-tuned Chl-a algorithms. For example, the OC3 algorithms adjusted for the Mediterranean Sea and the Red Sea (Santoleri et al., 2008; Brewin et al., 2015a), which represent warm waters, showed significantly lower ratios at a given Chl-a concentration compared to the OCMF. Similarly, the regional
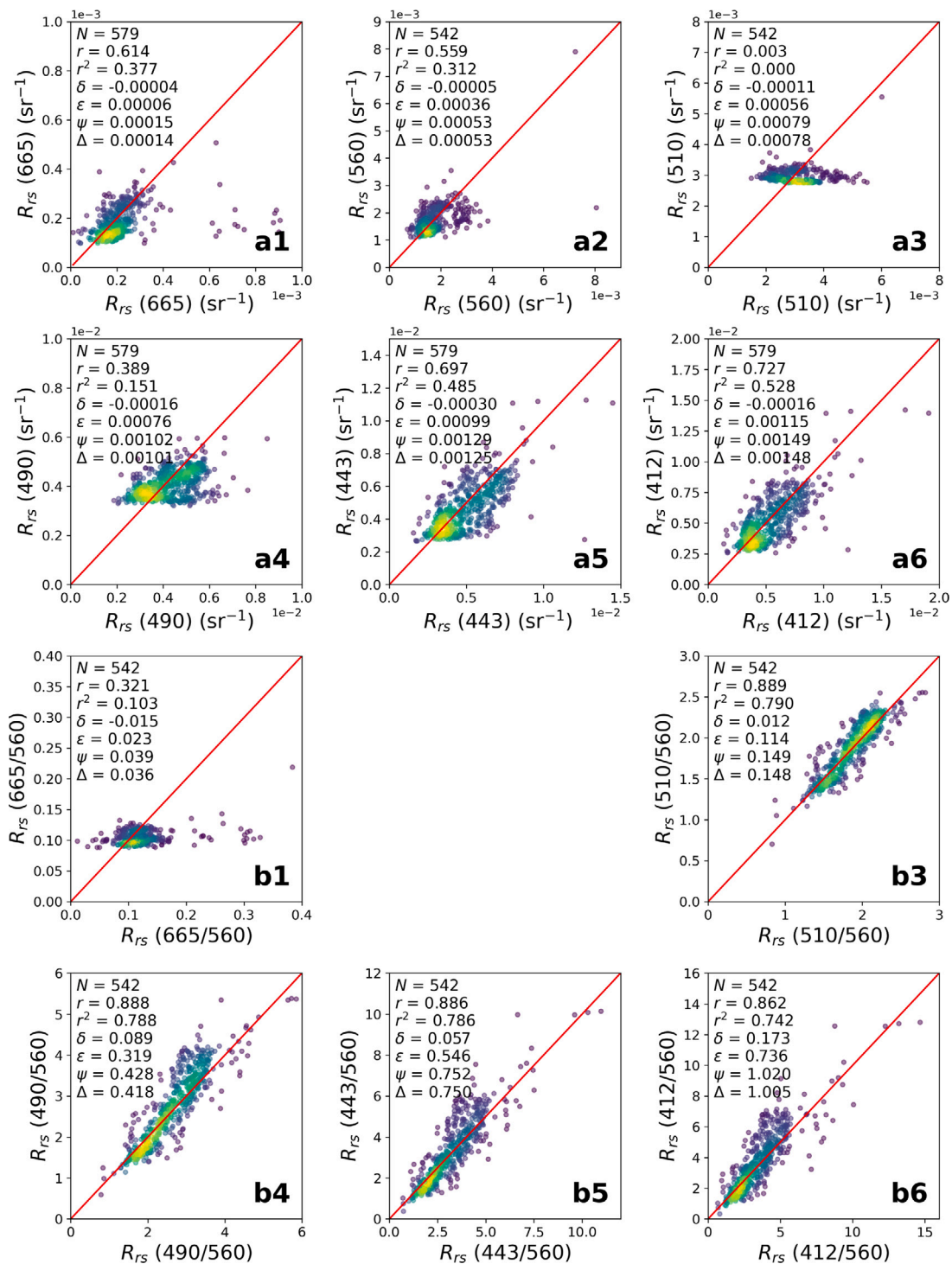
Fig. 9. Independent validation of R_{rs} between *in-situ* measurements (x-axis) and OCMF estimates (y-axis), $N = 579$. The a1–a6 are the magnitude of R_{rs}, and the b1–b6 are the R_{rs} normalised at 560 nm (b2 is missing because 560 nm is the denominator). The statistical tests are shown in each subplot. For R_{rs} magnitude, *p*-values are less than 0.05 for all wavelengths except 510 nm, while for R_{rs} ratio, *p*-values are less than 0.05 for all wavelengths. Red line refers to 1:1 line. Note that here the statistical test is computed in linear space, with the unit of sr^{-1} for magnitude and dimensionless for shape. The model is based on 16-parameter model (Sun et al., 2023). Results using the 17-parameter model are shown in Supplementary Figure S8. (For interpretation of the references to colour in this figure legend, the reader is referred to the web version of this article.)
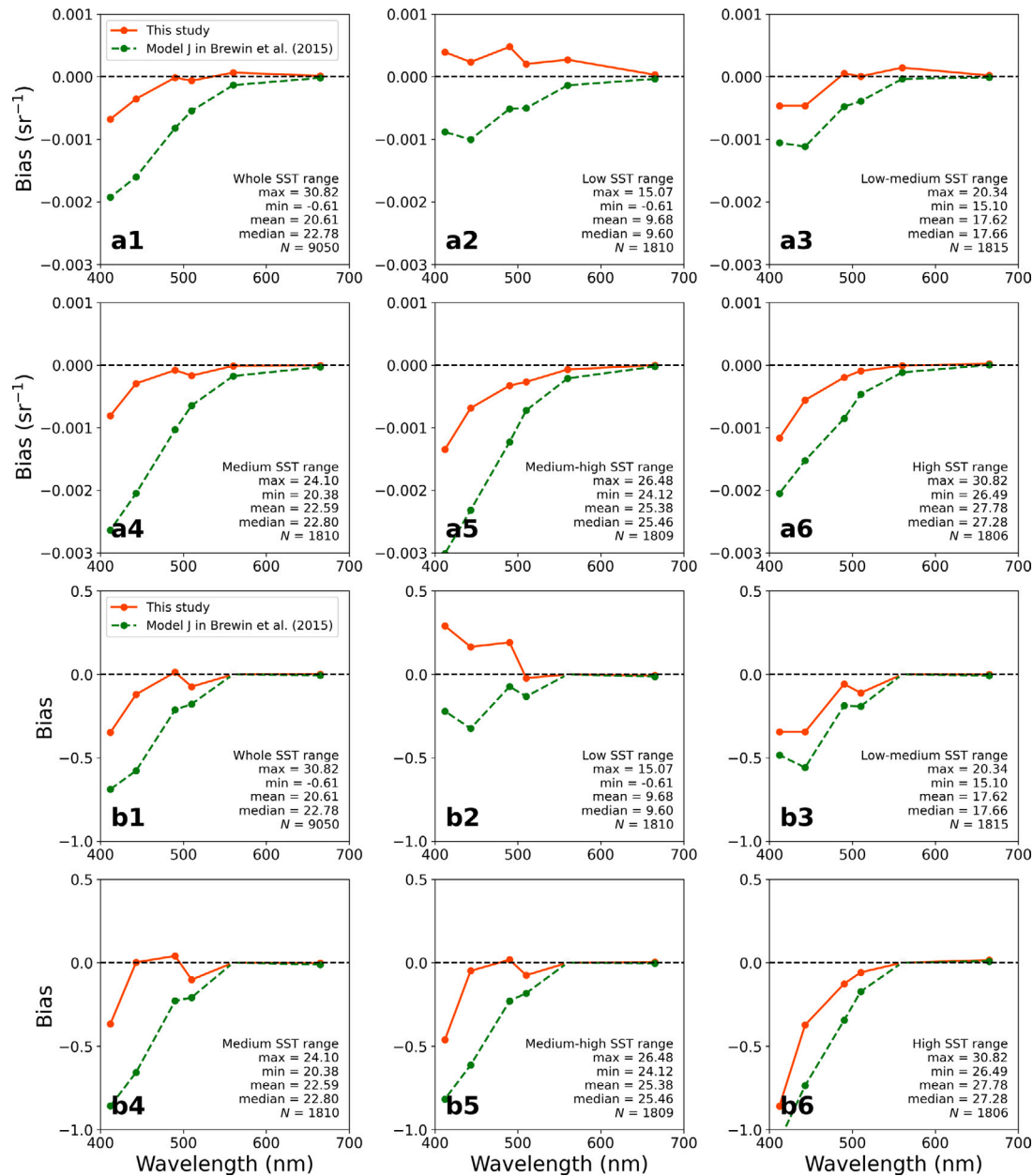
Fig. 10. The bias comparison of $R_{rs}(\lambda)$ between modelled and OC-CCI-derived values at six wavelengths, using the Graban et al. (2020) dataset ($N = 9050$). The OCMF is shown in red line, and Model J from Brewin et al. (2015b) is in green. The a1–a6 are the magnitude of R_{rs}, and the b1–b6 are the shape of R_{rs} normalised at 560 nm. Since 560 nm is used as the denominator in calculating the R_{rs} shape, the bias at 560 nm in b1–b6 is not displayed. The a1 (b1) refers to the whole dataset, while a2–a6 (b2–b6) represent results from sub-datasets divided into five temperature groups. Each sub-dataset includes approximately 1810 samples, with statistics of temperature shown in each subplot, with the unit of °C. Note that here the bias is computed in linear space, with the unit of sr^{-1} for magnitude and dimensionless for shape. The model is based on the 16-parameter model (Sun et al., 2023). Results using the 17-parameter model are shown in Supplementary Figure S9. (For interpretation of the references to colour in this figure legend, the reader is referred to the web version of this article.)

algorithms designed for the Arctic waters also exhibit lower band ratios (Lewis et al., 2016). These deviations were not accommodated by the OCMF. Previous studies suggested that the low band ratios in these regions could be caused by excess of CDOM concentration (Organelli et al., 2014; Kheireddine et al., 2018a; Lewis and Arrigo, 2020), compared to other open ocean waters. It is noteworthy that the proposed OCMF is designed for standard open ocean conditions and may not fully capture the influence of optically active components independent of phytoplankton on R_{rs} in specific regions. This highlights the importance of evaluating and potentially refining the OCMF to better account for the bio-optical characteristics of these unique environments.

4.4. Model applications

The OCMF presented in this study has been inspired by earlier work (Brewin et al., 2015a, 2019), which partitioned IOPs into different PSCs, based on the assumption that each class inhabits distinctive optical environments (Alvain et al., 2012). These IOPs show variations with Chl-a, representing the changes in bio-optical properties in waters due to the variations in phytoplankton size structure (Neukermans et al., 2016; Reynolds and Stramski, 2019). Meanwhile, temperature serves as an useful variable in predicting differences in optical properties for similar Chl-a concentrations, and may be useful to study
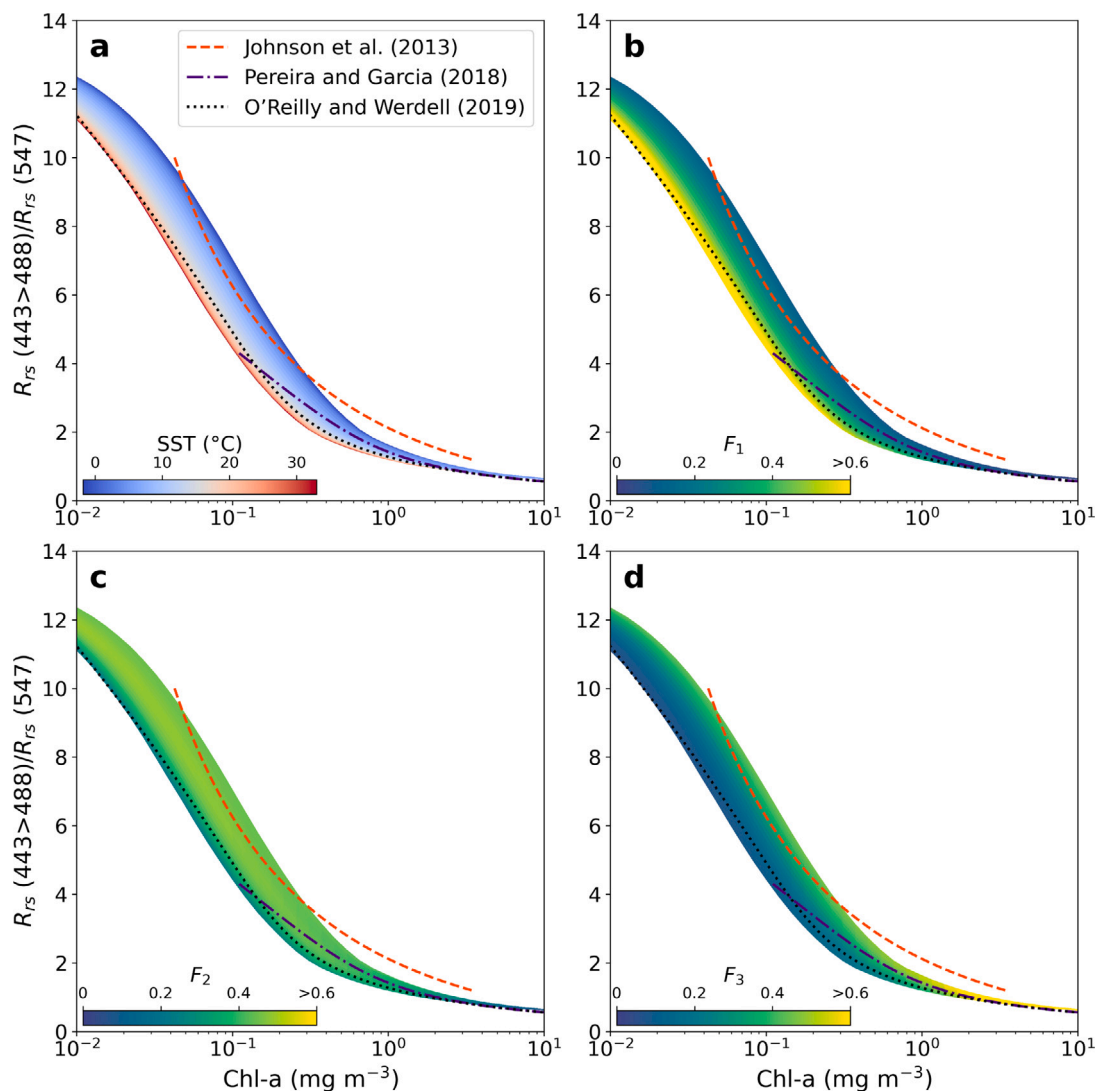
Fig. 11. The maximum band ratio of R_{rs} plotted against Chl-a, using the proposed OCMF and the simulated data, with Chl-a ranging from 0.01 to 10 mg m^{-3} and SST ranging from −1.8 to 33 °C. The coloured mesh plot represents the influence of SST variations on the maximum band ratio estimation (a), and fractions of each phytoplankton size class for the same model simulations (b–d). The F_1, F_2, and F_3 represent the fraction of pico-, nano-, and microplankton, respectively. The red dashed, purple dash-dot and black dotted lines represent the OC3 maximum band ratio algorithms of Johnson et al. (2013), Pereira and Garcia (2018) and O'Reilly and Werdell (2019), respectively. The model is based on the 16-parameter model (Sun et al., 2023). Results using the 17-parameter model are shown in Supplementary Figure S10. (For interpretation of the references to colour in this figure legend, the reader is referred to the web version of this article.)

effects of climate change on ocean colour (Sun et al., 2023). One can also consider OCMF as a flexible tool to explore how phytoplankton community structure impacts the reflectance spectrum. For example, it could be used to simulate the reflectance spectrum of an environment purely dominated by only one of the three size classes. This could be helpful in developing methods for detecting phytoplankton communities directly (Sathyendranath et al., 2004; Alvain et al., 2005), with future efforts potentially leveraging emerging hyperspectral ocean colour sensors (e.g., NASA PACE [Plankton, Aerosol, Cloud, ocean Ecosystem]). With the incorporation of the specific IOPs of phytoplankton community structure, the OCMF has potential to improve the description of optics in radiative transfer models (Bracher et al., 2017; Bi et al., 2023), and enhance our understanding of how light and optical constituents affect the ocean biogeochemistry (Xiu and Chai, 2014; Dutkiewicz et al., 2015; Álvarez et al., 2022).

The OCMF parameters (i.e., chlorophyll-specific IOPs) obtained in this study will serve as essential inputs, along with R_{rs} and SST measurements, for retrieving phytoplankton information (e.g., Chl-a) using inversion methods, which will be further explored in subsequent studies. The inversion process can simultaneously provide the bio-optical

properties, as well as their size fractions, from R_{rs}, significantly expanding the utility and applicability of the model. An increasing number of studies underscored the importance of employing IOPs to enhance our comprehension of biogeochemical cycles (Werdell et al., 2018, and references therein). The b_{bph} and b_{bd} models (Section 3.3.2) could offer valuable insights in characterising particulate assemblages and understanding their impact on the backscattering coefficient, potentially aiding in the analysis of phytoplankton carbon and suspended particulate matter (Brewin et al., 2023b). By considering independent changes in size structure for the same Chl-a, the ambiguity problem (Defoin-Platel and Chami, 2007) might be better constrained in the open ocean.

The forward OCMF mainly focuses on the open ocean, where IOPs can be tied to phytoplankton, represented by Chl-a (Morel and Prieur, 1977). However, climate change can have an impact on a variety of water bodies, such as coastal regions that contribute significant amounts of non-algal substances (van Oostende et al., 2023). Consequently, how the model can be adapted to diverse aquatic environments needs to be considered. In future inverse modelling, spectral-independent multiplicative factors which capture an excess or deficit of non-algal

substance will be introduced, akin to the parameter Φ in Morel and Gentili (2009). They can address potential overestimation or underestimation of the model parameters when applied to waters with different bio-optical properties. In the oceanic waters, for example, these factors are likely to be close to one, indicating that the model performs well without adjustments. However, in coastal waters with substantial non-algal substances, these factors are likely to exceed one, as seen in the Red Sea and Mediterranean Sea (Brewin et al., 2015a; Pérez et al., 2016). This approach may extend the applicability of the model to diverse water types worldwide.

The development of OCMF relies on global standard ocean conditions, and its focus on synoptic patterns raises concerns about its ability to accurately represent higher spatial and temporal variability. For example, the OCMF may not adequately capture the unique bio-optical characteristics of specific regions, such as coastal waters with high suspended sediment concentrations or marginal seas with elevated CDOM levels (D'Sa et al., 2006; Naik et al., 2013). Additionally, escalating extreme events under climate change such as algal blooms and wildfire can significantly alter bio-optics (Zhao et al., 2009; Li et al., 2021), which are not currently validated within the proposed OCMF. Moreover, the OCMF does not consider short-term fluctuations, such as diel changes in phytoplankton responses to temperature, which can affect optical properties (Kheireddine and Antoine, 2014; Poulin et al., 2018). It is worth noting that the OCMF may not provide optimal performance under all circumstances and across all water types globally. However, ongoing efforts will be made to refine the model and adapt it as more data become available.

5. Summary

We compiled the most extensive global (to the best of our knowledge) *in-situ* dataset of optical properties within the surface ocean (≤ 20 m depth). The dataset spans from 1994 to 2021 and includes 47,295 samples, gathered from various sources. It comprises independent datasets with IOPs including absorption (a_{ph}, a_d, a_g) and backscattering (b_{bp}) coefficients, as well as remote sensing reflectance (R_{rs}). These datasets are accompanied by concurrent *in-situ* Chl-a and OISST-derived SST, and were divided into training (pre 2016) and validation (post 2016) datasets to ensure independent validation.

Using the training dataset, we developed a forward modelling framework (OCMF) that can estimate R_{rs} in open ocean waters for any given pair of Chl-a and SST measurements. The basis of the OCMF is the integration of the absorption and backscattering coefficients of each water constituent, all of which (except for water itself) respond to changes in Chl-a and temperature. To achieve this, we integrated the ecological model (Sun et al., 2023) that partitions phytoplankton into three size classes. We also accounted for the effect of a background of non-algal particles on ocean optics. Each IOP within the model was parameterised and independently validated, and found to compare favourably with conventional models from previous studies. Chlorophyll-specific IOPs were assigned to each size class in the OCMF. When compared with a previous forward model, the OCMF shows advantages in estimating R_{rs} with higher accuracy under varying temperature conditions.

The development of the OCMF is a critical component for establishing a Chl-a algorithm that is more considerate of the impact of climate change on ocean colour. Serving as a link between ecological concepts and optical models, the OCMF provides essential model parameters with both biological and optical significance for the forthcoming inversion model. It expands the scope of forward ocean colour modelling by addressing potential ambiguity in ocean-colour data. Subsequent studies will involve monitoring the variability of phytoplankton and their size distribution over long periods to better understand their responses to climate change.

Declaration of competing interest

The authors declare that they have no known competing financial interests or personal relationships that could have appeared to influence the work reported in this paper.

Appendix A

See Table A.1.

Table A.1

Definitions of the abbreviations and symbols used in this manuscript.

Abbreviation symbol	Definition	Units ('\' indicates an abbreviation)
BRDF	Bidirectional reflectance distribution function	\
CDOM	Coloured dissolved organic matter	\
Chl-a	Chlorophyll-a concentration	mg m^{-3}
HPLC	High performance liquid chromatography	\
NAP	Non-algal particles	\
OCMF	Ocean Colour Modelling Framework	\
OC-CCI	Ocean Colour Climate Change Initiative	\
OISST	Optimal Interpolation Sea Surface Temperature	\
PSCs	Phytoplankton size classes	\
SST	Sea surface temperature	°C
$a(\lambda)$	Total absorption coefficient	m^{-1}
$a_d(\lambda)$	Absorption coefficient of non-algal particles	m^{-1}
$a_d^k(\lambda)$	Absorption coefficient of background of non-algal particles	m^{-1}
$a_d^*(\lambda)$	Chlorophyll-specific absorption coefficient of non-algal particles	m^2 (mg C)$^{-1}$
$a_g(\lambda)$	Absorption coefficient of coloured dissolved organic matter	m^{-1}
$a_g^*(\lambda)$	Chlorophyll-specific absorption coefficient of coloured dissolved organic matter	m^2 (mg C)$^{-1}$
$a_p(\lambda)$	Absorption coefficient of particles	m^{-1}
$a_{ph}(\lambda)$	Absorption coefficient of phytoplankton	m^{-1}
$a_{ph}^*(\lambda)$	Chlorophyll-specific absorption coefficient of phytoplankton	m^2 (mg C)$^{-1}$
$a_w(\lambda)$	Absorption coefficient of water	m^{-1}
$b_{bd}(\lambda)$	Backscattering coefficient of non-algal particles	m^{-1}
$b_{bd}^*(\lambda)$	Chlorophyll-specific backscattering coefficient of non-algal particles	m^2 (mg C)$^{-1}$
$b_{bp}^k(\lambda)$	Backscattering coefficient of background of non-algal particles	m^{-1}
$b_{bp}(\lambda)$	Backscattering coefficient of particles	m^{-1}
$b_{bp}^*(\lambda)$	Chlorophyll-specific backscattering coefficient of particles	m^2 (mg C)$^{-1}$
$b_{bph}(\lambda)$	Backscattering coefficient of phytoplankton	m^{-1}
$b_{bph}^*(\lambda)$	Chlorophyll-specific backscattering coefficient of phytoplankton	m^2 (mg C)$^{-1}$
$b_{bw}(\lambda)$	Backscattering coefficient of water	m^{-1}
C	In-situ Chl-a concentration	mg m^{-3}
C_1, C_2, C_3, $C_{1,2}$	Chl-a concentration of picoplankton, nanoplankton, microplankton, and combined pico- and nanoplankton	mg m^{-3}
$C_{1,2}^m$, C_1^m	Asymptotic maximum values for combined pico- and nanoplankton and picoplankton	mg m^{-3}
$D_{1,2}$, D_1	Fraction of Chl-a as total Chl-a tends to zero for combined pico- and nanoplankton and picoplankton	Dimensionless
F_1, F_2, F_3, $F_{1,2}$	Fraction of Chl-a for picoplankton, nanoplankton, microplankton, and combined pico- and nanoplankton	Dimensionless
G_a, G_b, G_c, G_d	Parameters for $C_{1,2}^m$ in 16-parameter model, where G_a and G_d control the upper and lower bounds, G_b represents the slope of the change, G_c is the SST mid-point of slope	mg m^{-3}, °C^{-1}, °C, mg m^{-3}
$G_0^w(\Omega)$, $G_1^w(\Omega)$, $G_0^p(\Omega)$, $G_1^p(\Omega)$	Parameters for the optical model of Lee et al. (2013)	sr^{-1}
H_a, H_b, H_c, H_d	Parameters for C_1^m in 16-parameter model, same as G_a-G_d	mg m^{-3}, °C^{-1}, °C, mg m^{-3}
i	i = 1, 2, and 3 for pico-, nano-, and microplankton	\
J_a, J_b, J_c, J_d	Parameters for $D_{1,2}$ in 16-parameter model, same as G_a-G_d	Dimensionless, °C^{-1}, °C, dimensionless
O_a, O_b, O_c, O_d	Parameters for D_1 in 16-parameter model, same as G_a-G_d	Dimensionless, °C^{-1}, °C, dimensionless
p	p-value	Dimensionless
r	Pearson linear correlation coefficient	Dimensionless
$R_{rs}(\lambda)$	Remote sensing reflectance	sr^{-1}
r^2	Coefficient of determination, r-squared	Dimensionless
S_d	Slope of non-algal particles absorption	nm^{-1}
S_d^k	Slope of background of non-algal particles absorption	nm^{-1}
S_g	Slope of coloured dissolved organic matter absorption	nm^{-1}
U_a, U_b, U_c	Parameters for $C_{1,2}^m$ in 17-parameter model	mg m^{-3} °C^{-2}, mg m^{-3} °C^{-1}, mg m^{-3}

Table A.1 (*continued*).

Abbreviation symbol	Definition	Units ('\' indicates an abbreviation)
$V_a, V_b, V_c, V_d, V_e, V_f$	Parameters for C_1^m in 17-parameter model, V_a and V_d are the height of peaks, V_b and V_e are the positions of peak centres, and V_c and V_f control the width of the curve	mg m^{-3}, °C, °C, mg m^{-3}, °C, °C
γ	Slope of particulate backscattering	Dimensionless
$\gamma_{d,i}$	Slope of non-algal particulate backscattering	Dimensionless
$\gamma_{ph,i}$	Slope of phytoplankton backscattering	Dimensionless
δ	Bias	The unit depends on the input
Δ	Centre-patterned root mean square difference	The unit depends on the input
ϵ	MAD, mean absolute difference	The unit depends on the input
κ	The total of absorption and backscattering coefficient	m^{-1}
λ	Wavelength	nm
λ_0	Reference wavelength	nm
ψ	RMSD, root mean squared difference	The unit depends on the input
Ω	Sun-sensor angular geometry for R_{rs}	Rad

Appendix B. Supplementary data

Supplementary material related to this article can be found online at https://doi.org/10.1016/j.rse.2024.114487.

Data availability

Data will be made available on request.

References

Ahn, Y.-H., Bricaud, A., Morel, A., 1992. Light backscattering efficiency and related properties of some phytoplankters. Deep Sea Res. Part A. Oceanogr. Res. Pap. 39 (11–12), 1835–1855. http://dx.doi.org/10.1016/0198-0149(92)90002-B.

Alvain, S., Loisel, H., Dessailly, D., 2012. Theoretical analysis of ocean color radiances anomalies and implications for phytoplankton groups detection in case 1 waters. Opt. Express 20 (2), 1070. http://dx.doi.org/10.1364/OE.20.001070.

Alvain, S., Moulin, C., Dandonneau, Y., Bréon, F., 2005. Remote sensing of phytoplankton groups in case 1 waters from global SeaWiFS imagery. Deep Sea Res. Part I: Oceanogr. Res. Pap. 52 (11), 1989–2004. http://dx.doi.org/10.1016/j.dsr.2005.06.015.

Alvain, S., Moulin, C., Dandonneau, Y., Loisel, H., 2008. Seasonal distribution and succession of dominant phytoplankton groups in the global ocean: A satellite view. Glob. Biogeochem. Cycles 22 (3), n/a–n/a. http://dx.doi.org/10.1029/2007GB003154.

Álvarez, E., Losa, S.N., Bracher, A., Thoms, S., Völker, C., 2022. Phytoplankton light absorption impacted by photoprotective carotenoids in a global ocean spectrally-resolved biogeochemistry model. J. Adv. Modelling Earth Syst. 14 (11), http://dx.doi.org/10.1029/2022MS003126.

Antoine, D., Chami, M., Claustre, H., d'Ortenzio, F., Morel, A., Bécu, G., Gentili, B., Louis, F., Ras, J., Roussier, E., Scott, A.J., Tailliez, D., Hooker, S.B., Guevel, P., Desté, J.-F., Dempsey, C., Adams, D., 2006. BOUSSOLE: A Joint CNRS-INSU, ESA, CNES, and NASA ocean color calibration and validation activity. Tech. rep., National Aeronautics and Space Administration, URL https://ntrs.nasa.gov/citations/20070028812.

Antoine, D., Guevel, P., Desté, J.-F., Bécu, G., Louis, F., Scott, A.J., Bardey, P., 2008. The "BOUSSOLE" Buoy—A new transparent-to-swell taut mooring dedicated to marine optics: Design, tests, and performance at sea. J. Atmos. Ocean. Technol. 25 (6), 968–989. http://dx.doi.org/10.1175/2007JTECHO563.1.

Ardyna, M., Arrigo, K.R., 2020. Phytoplankton dynamics in a changing Arctic Ocean. Nature Clim. Change 10 (10), 892–903. http://dx.doi.org/10.1038/s41558-020-0905-y.

Arrigo, K.R., Robinson, D.H., Worthen, D.L., Schieber, B., Lizotte, M.P., 1998. Bio-optical properties of the southwestern Ross Sea. J. Geophys. Res.: Oceans 103 (C10), 21683–21695. http://dx.doi.org/10.1029/98JC02157.

Babin, M., Stramski, D., Ferrari, G.M., Claustre, H., Bricaud, A., Obolensky, G., Hoepffner, N., 2003. Variations in the light absorption coefficients of phytoplankton, nonalgal particles, and dissolved organic matter in coastal waters around Europe. J. Geophys. Res. 108 (C7), http://dx.doi.org/10.1029/2001JC000882.

Balch, W.M., Holligan, P.M., Ackleson, S.G., Voss, K.J., 1991. Biological and optical properties of mesoscale coccolithophore blooms in the Gulf of Maine. Limnol. Oceanogr. 36 (4), 629–643. http://dx.doi.org/10.4319/lo.1991.36.4.0629.

Barbieux, M., Uitz, J., Bricaud, A., Organelli, E., Poteau, A., Schmechtig, C., Gentili, B., Obolensky, G., Leymarie, E., Penkerc'h, C., D'Ortenzio, F., Claustre, H., 2018. Assessing the variability in the relationship between the particulate backscattering coefficient and the chlorophyll a concentration from a global biogeochemical-argo database. J. Geophys. Res.: Oceans 123 (2), 1229–1250. http://dx.doi.org/10.1002/2017JC013030.

Barlow, R.G., Aiken, J., Holligan, P.M., Cummings, D.G., Maritorena, S., Hooker, S., 2002. Phytoplankton pigment and absorption characteristics along meridional transects in the Atlantic Ocean. Deep Sea Res. Part I: Oceanogr. Res. Pap. 49 (4), 637–660. http://dx.doi.org/10.1016/S0967-0637(01)00081-4.

Barlow, R., Kyewalyanga, M., Sessions, H., van den Berg, M., Morris, T., 2008. Phytoplankton pigments, functional types, and absorption properties in the Delagoa and Natal Bights of the Agulhas ecosystem. Estuar. Coast. Shelf Sci. 80 (2), 201–211. http://dx.doi.org/10.1016/j.ecss.2008.07.022.

Barlow, R., Lamont, T., Kyewalyanga, M., Sessions, H., van den Berg, M., Duncan, F., 2011. Phytoplankton production and adaptation in the vicinity of Pemba and Zanzibar islands, Tanzania. Afr. J. Mar. Sci. 33 (2), 283–295. http://dx.doi.org/10.2989/1814232X.2011.600430.

Behrenfeld, M.J., Boss, E., Siegel, D.A., Shea, D.M., 2005. Carbon-based ocean productivity and phytoplankton physiology from space. Glob. Biogeochem. Cycles 19 (1), http://dx.doi.org/10.1029/2004GB002299.

Bellacicco, M., Cornec, M., Organelli, E., Brewin, R.J.W., Neukermans, G., Volpe, G., Barbieux, M., Poteau, A., Schmechtig, C., D'Ortenzio, F., Marullo, S., Claustre, H., Pitarch, J., 2019. Global variability of optical backscattering by non-algal particles from a biogeochemical-argo data set. Geophys. Res. Lett. 46 (16), 9767–9776. http://dx.doi.org/10.1029/2019GL084078.

Bi, S., Hieronymi, M., Röttgers, R., 2023. Bio-geo-optical modelling of natural waters. Front. Mar. Sci. 10, http://dx.doi.org/10.3389/fmars.2023.1196352.

Blondeau-Patissier, D., Gower, J.F.R., Dekker, A.G., Phinn, S.R., Brando, V.E., 2014. A review of ocean color remote sensing methods and statistical techniques for the detection, mapping and analysis of phytoplankton blooms in coastal and open oceans. Prog. Oceanogr. 123, 123–144. http://dx.doi.org/10.1016/j.pocean.2013.12.008.

Boss, E.S., Collier, R., Larson, G., Fennel, K., Pegau, W.S., 2007. Measurements of spectral optical properties and their relation to biogeochemical variables and processes in Crater Lake, Crater Lake National Park, OR. Hydrobiologia 574 (1), 149–159. http://dx.doi.org/10.1007/s10750-006-2609-3.

Boss, E., Picheral, M., Searson, S., Marec, C., Le Goff, H., Reverdin, G., Leeuw, T., Chase, A., Anderson, L., Gattuso, J.-P., Pino, D.R., Gyllencreutz, R., Grondin, P.-L., Matuoka, A., Babin, M., Bricaud, A., Taillandier, V., Hafez, M., Chekalyuk, A., Pesant, S., 2017. Underway surface water data during the Tara Oceans expedition in 2013. http://dx.doi.org/10.1594/PANGAEA.873567.

Bouman, H.A., Platt, T., Sathyendranath, S., Li, W.K.W., Stuart, V., Fuentes-Yaco, C., Maass, H., Horne, E.P.W., Ulloa, O., Lutz, V., Kyewalyanga, M., 2003. Temperature as indicator of optical properties and community structure of marine phytoplankton: implications for remote sensing. Mar. Ecol. Progr. Ser. 258, 19–30. http://dx.doi.org/10.3354/meps258019.

Boyce, D.G., Lewis, M.R., Worm, B., 2010. Global phytoplankton decline over the past century. Nature 466 (7306), 591–596. http://dx.doi.org/10.1038/nature09268.

Bracher, A., 2014a. Phytoplankton pigment concentrations during POLARSTERN cruise ANT-XXVIII/3. http://dx.doi.org/10.1594/PANGAEA.848588.

Bracher, A., 2014b. Phytoplankton pigments measured on water bottle samples during SONNE cruise SO218. http://dx.doi.org/10.1594/PANGAEA.848589.

Bracher, A., 2015. Phytoplankton pigment concentrations during POLARSTERN cruise ANT-XXVI/4. http://dx.doi.org/10.1594/PANGAEA.848585.

Bracher, A., 2017a. Remote sensing reflectance during POLARSTERN cruise ANT-XXV/1. http://dx.doi.org/10.1594/PANGAEA.879225.

Bracher, A., 2017b. Remote sensing reflectance during POLARSTERN cruise ANT-XXVI/4. http://dx.doi.org/10.1594/PANGAEA.879226.

Bracher, A., 2019. Phytoplankton pigment concentrations in the Southern Ocean during RV POLARSTERN cruise PS103 in Dec 2016 to Jan 2017. http://dx.doi.org/10.1594/PANGAEA.898941.

Bracher, A., Bouman, H.A., Brewin, R.J.W., Bricaud, A., Brotas, V., Ciotti, A.M., Clementson, L., Devred, E., Di Cicco, A., Dutkiewicz, S., Hardman-Mountford, N.J., Hickman, A.E., Hieronymi, M., Hirata, T., Losa, S.N., Mouw, C.B., Organelli, E.,

Raitsos, D.E., Uitz, J., Vogt, M., Wolanin, A., 2017. Obtaining phytoplankton diversity from ocean color: A scientific roadmap for future development. Front. Mar. Sci. 4, http://dx.doi.org/10.3389/fmars.2017.00055.

Bracher, A., Cheah, W., 2022. Remote sensing reflectance measured in the South China Sea and Sulu Sea during RV Sonne cruise SO218 from 18 to 27 November 2011. http://dx.doi.org/10.1594/PANGAEA.946368.

Bracher, A., Gonçalves-Araujo, R., Dinter, T., Cherkasheva, A., 2018. Remote sensing reflectance obtained from spectral underwater upwelling radiance and in air solar downwelling irradiance measurements during POLARSTERN cruise ARK-XXVI/3 (PS78). http://dx.doi.org/10.1594/PANGAEA.884526.

Bracher, A., Liu, Y., 2021a. Spectrophotometric measurements of absorption coefficients by non-algal particles in the Atlantic Southern Ocean during RV POLARSTERN cruise PS103 in Dec 2016 to Jan 2017. http://dx.doi.org/10.1594/PANGAEA.938196.

Bracher, A., Liu, Y., 2021b. Spectrophotometric measurements of absorption coefficients by phytoplankton in the Atlantic Southern Ocean during RV POLARSTERN cruise PS103 in Dec 2016 to Jan 2017. http://dx.doi.org/10.1594/PANGAEA.938193.

Bracher, A., Liu, Y., Hellmann, S., Bensi, M., Kovacevic, V., Röttgers, R., 2021a. Absorption coefficients by coloured dissolved organic matter from North Sea to Fram Strait measured at fixed stations with a Liquid Waveguide Capillary Cell system during POLARSTERN cruise PS99.1. http://dx.doi.org/10.1594/PANGAEA.938491.

Bracher, A., Liu, Y., Hellmann, S., Röttgers, R., 2021b. Absorption coefficients by coloured dissolved organic matter from North Sea to Fram Strait measured underway with a Liquid Waveguide Capillary Cell system during POLARSTERN cruise PS99.1. http://dx.doi.org/10.1594/PANGAEA.938494.

Bracher, A., Liu, Y., Oelker, J., Röttgers, R., 2021c. Absorption coefficients by coloured dissolved organic matter across the South Atlantic Ocean measured underway with a Liquid Waveguide Capillary Cell system during POLARSTERN cruise PS103. http://dx.doi.org/10.1594/PANGAEA.938468.

Bracher, A., Liu, Y., Wiegmann, S., 2021d. Spectrophotometric measurements of absorption coefficients by non-algal particles during during HEINCKE cruise HE462 in the North Sea and Sogne Fjord from 29 April to 7 May 2016. http://dx.doi.org/10.1594/PANGAEA.938152.

Bracher, A., Liu, Y., Wiegmann, S., 2021e. Spectrophotometric measurements of absorption coefficients by non-algal particles during RV POLARSTERN cruise PS121 from 11 Aug to 10 Sep 2019. http://dx.doi.org/10.1594/PANGAEA.938262.

Bracher, A., Liu, Y., Wiegmann, S., 2021f. Spectrophotometric measurements of absorption coefficients by phytoplankton during HEINCKE cruise HE462 in the North Sea and Sogne Fjord from 29 April to 7 May 2016. http://dx.doi.org/10.1594/PANGAEA.938153.

Bracher, A., Liu, Y., Wiegmann, S., 2021g. Spectrophotometric measurements of absorption coefficients by phytoplankton during RV POLARSTERN cruise PS121 from 11 Aug to 10 Sep 2019. http://dx.doi.org/10.1594/PANGAEA.938260.

Bracher, A., Liu, Y., Wiegmann, S., Röttgers, R., 2021h. Absorption coefficients by coloured dissolved organic matter (CDOM) from North Sea to Fram Strait measured at fixed stations with a Liquid Waveguide Capillary Cell system during POLARSTERN cruise PS121. http://dx.doi.org/10.1594/PANGAEA.938472.

Bracher, A., Liu, Y., Wiegmann, S., Röttgers, R., 2021i. Absorption coefficients by coloured dissolved organic matter (CDOM) from North Sea to Fram Strait measured underway with a Liquid Waveguide Capillary Cell system during POLARSTERN cruise PS121. http://dx.doi.org/10.1594/PANGAEA.938491.

Bracher, A., Liu, Y., Wiegmann, S., Röttgers, R., 2021j. Absorption coefficients by coloured dissolved organic matter obtained at fixed stations with a Liquid Waveguide Capillary Cell system during HEINCKE cruise HE462 in the North Sea and Sogne Fjord. http://dx.doi.org/10.1594/PANGAEA.938383.

Bracher, A., Liu, Y., Wiegmann, S., Röttgers, R., 2021k. Absorption coefficients by coloured dissolved organic matter obtained underway with a Liquid Waveguide Capillary Cell system during HEINCKE cruise HE462 in the North Sea and Sogne Fjord. http://dx.doi.org/10.1594/PANGAEA.938384.

Bracher, A., Liu, Y., Xi, H., Wiegmann, S., 2021l. Spectrophotometric measurements of absorption coefficients by non-algal particles during POLARSTERN cruise PS113 along an Atlantic Transect. http://dx.doi.org/10.1594/PANGAEA.938185.

Bracher, A., Röttgers, R., 2022. Remote sensing reflectance measured in the Peruvian Coast and upwelling area during RV Sonne cruise SO243 from 12 to 19 October 2015. http://dx.doi.org/10.1594/PANGAEA.946394.

Bracher, A., Taylor, B.B., 2021a. Particulate absorption during POLARSTERN cruise ANT-XXVI/4 (PS75). http://dx.doi.org/10.1594/PANGAEA.936547.

Bracher, A., Taylor, B.B., 2021b. Phytoplankton absorption during POLARSTERN cruise ANT-XXVI/4 (PS75). http://dx.doi.org/10.1594/PANGAEA.937971.

Bracher, A., Taylor, B.B., Cheah, W., 2021m. Particulate absorption during RV Sonne expedition SO218. http://dx.doi.org/10.1594/PANGAEA.936553.

Bracher, A., Taylor, B.B., Cheah, W., 2021n. Phytoplankton absorption during SONNE cruise SO218. http://dx.doi.org/10.1594/PANGAEA.937982.

Bracher, A., Taylor, M.H., Taylor, B.B., Dinter, T., Röttgers, R., Steinmetz, F., 2015. Phytoplankton pigment concentrations during POLARSTERN cruise ANT-XXIII/1. http://dx.doi.org/10.1594/PANGAEA.871713.

Bracher, A., Tilzer, M., 2001. Underwater light field and phytoplankton absorbance in different surface water masses of the Atlantic sector of the Southern Ocean. Polar Biol. 24 (9), 687–696. http://dx.doi.org/10.1007/s003000100269.

Bracher, A., Vountas, M., Dinter, T., Burrows, J.P., Röttgers, R., Peeken, I., 2009. Quantitative observation of cyanobacteria and diatoms from space using PhytoDOAS on SCIAMACHY data. Biogeosciences 6 (5), 751–764. http://dx.doi.org/10.5194/bg-6-751-2009.

Bracher, A., Wiegmann, S., 2019. Phytoplankton pigment concentrations in the North Sea and Sogne Fjord from 29 April to 7 May 2016 during RV HEINCKE cruise HE462. http://dx.doi.org/10.1594/PANGAEA.899043.

Bracher, A., Wiegmann, S., 2022a. Phytoplankton pigment concentrations during POLARSTERN cruise PS121 from North Sea to Fram in August to September 2019. http://dx.doi.org/10.1594/PANGAEA.941011.

Bracher, A., Wiegmann, S., 2022b. Remote sensing reflectance measured at discrete underwater profile stations in the North Sea during RV HEINCKE cruise HE462 from 30 April to 7 May 2016. http://dx.doi.org/10.1594/PANGAEA.944796.

Bracher, A., Wiegmann, S., Xi, H., Dinter, T., 2020. Phytoplankton pigment concentration and phytoplankton groups measured on water samples obtained during POLARSTERN cruise PS113 in the Atlantic Ocean. http://dx.doi.org/10.1594/PANGAEA.911061.

Brewin, R.J.W., Ciavatta, S., Sathyendranath, S., Jackson, T., Tilstone, G., Curran, K., Airs, R.L., Cummings, D., Brotas, V., Organelli, E., Dall'Olmo, G., Raitsos, D.E., 2017. Uncertainty in ocean-color estimates of chlorophyll for phytoplankton groups. Front. Mar. Sci. 4, http://dx.doi.org/10.3389/fmars.2017.00104, URL https://www.frontiersin.org/article/10.3389/fmars.2017.00104.

Brewin, R.J.W., Ciavatta, S., Sathyendranath, S., Skákala, J., Bruggeman, J., Ford, D., Platt, T., 2019. The influence of temperature and community structure on light absorption by phytoplankton in the north atlantic. Sensors 19 (19), 4182. http://dx.doi.org/10.3390/s19194182.

Brewin, R.J.W., Dall'Olmo, G., Sathyendranath, S., Hardman-Mountford, N.J., 2012. Particle backscattering as a function of chlorophyll and phytoplankton size structure in the open-ocean. Opt. Express 20 (16), 17632. http://dx.doi.org/10.1364/OE.20.017632.

Brewin, R.J.W., Devred, E., Sathyendranath, S., Lavender, S.J., Hardman-Mountford, N.J., 2011. Model of phytoplankton absorption based on three size classes. Appl. Opt. 50 (22), 4535. http://dx.doi.org/10.1364/AO.50.004535.

Brewin, R.J.W., Pitarch, J., Dall'Olmo, G., van der Woerd, H.J., Lin, J., Sun, X., Tilstone, G.H., 2023a. Evaluating historic and modern optical techniques for monitoring phytoplankton biomass in the Atlantic Ocean. Front. Mar. Sci. 10, http://dx.doi.org/10.3389/fmars.2023.1111416.

Brewin, R.J.W., Raitsos, D.E., Dall'Olmo, G., Zarokanellos, N., Jackson, T., Racault, M.-F., Boss, E.S., Sathyendranath, S., Jones, B.H., Hoteit, I., 2015a. Regional ocean-colour chlorophyll algorithms for the Red Sea. Remote Sens. Environ. 165, 64–85. http://dx.doi.org/10.1016/j.rse.2015.04.024.

Brewin, R.J.W., Sathyendranath, S., Bricaud, A., Ciotti, A., Devred, E., Hirata, T., Kostadinov, T.S., Loisel, H., Mouw, C.B., Uitz, J., 2014. Detection of phytoplankton size structure by remote sensing. In: Sathyendranath, S. (Ed.), Phytoplankton Functional Types from Space. Reports of the International Ocean-Colour Coordinating Group, No. 15, IOCCG, Dartmouth, Canada., pp. 71–100.

Brewin, R.J.W., Sathyendranath, S., Hirata, T., Lavender, S.J., Barciela, R.M., Hardman-Mountford, N.J., 2010. A three-component model of phytoplankton size class for the Atlantic Ocean. Ecol. Model. 221 (11), 1472–1483. http://dx.doi.org/10.1016/j.ecolmodel.2010.02.014.

Brewin, R.J.W., Sathyendranath, S., Kulk, G., Rio, M.-H., Concha, J.A., Bell, T.G., Bracher, A., Fichot, C., Frölicher, T.L., Galí, M., Hansell, D.A., Kostadinov, T.S., Mitchell, C., Neeley, A.R., Organelli, E., Richardson, K., Rousseaux, C., Shen, F., Stramski, D., Tzortziou, M., Watson, A.J., Addey, C.I., Bellacicco, M., Bouman, H., Carroll, D., Cetinić, I., Dall'Olmo, G., Frouin, R., Hauck, J., Hieronymi, M., Hu, C., Ibello, V., Jönsson, B., Kong, C.E., Kovač, Ž., Laine, M., Lauderdale, J., Lavender, S., Livanou, E., Llort, J., Lorinczi, L., Nowicki, M., Pradisty, N.A., Psarra, S., Raitsos, D.E., Ruescas, A.B., Russell, J.L., Salisbury, J., Sanders, R., Shutler, J.D., Sun, X., Taboada, F.G., Tilstone, G.H., Wei, X., Woolf, D.K., 2023b. Ocean carbon from space: Current status and priorities for the next decade. Earth-Sci. Rev. 240, 104386. http://dx.doi.org/10.1016/j.earscirev.2023.104386.

Brewin, R.J.W., Sathyendranath, S., Müller, D., Brockmann, C., Deschamps, P.-Y., Devred, E., Doerffer, R., Fomferra, N., Franz, B., Grant, M., Groom, S., Horseman, A., Hu, C., Krasemann, H., Lee, Z., Maritorena, S., Mélin, F., Peters, M., Platt, T., Regner, P., Smyth, T., Steinmetz, F., Swinton, J., Werdell, J., White, G.N., 2015b. The ocean colour climate change initiative: III. a round-robin comparison on in-water bio-optical algorithms. Remote Sens. Environ. 162, 271–294. http://dx.doi.org/10.1016/j.rse.2013.09.016.

Bricaud, A., Babin, M., Claustre, H., Ras, J., Tièche, F., 2010. Light absorption properties and absorption budget of Southeast Pacific waters. J. Geophys. Res. 115 (C8), http://dx.doi.org/10.1029/2009jc005517.

Bricaud, A., Babin, M., Morel, A., Claustre, H., 1995. Variability in the chlorophyll-specific absorption coefficients of natural phytoplankton: Analysis and parameterization. J. Geophys. Res. 100 (C7), 13321. http://dx.doi.org/10.1029/95JC00463.

Bricaud, A., Ciotti, A.M., Gentili, B., 2012. Spatial-temporal variations in phytoplankton size and colored detrital matter absorption at global and regional scales, as derived from twelve years of SeaWiFS data (1998–2009). Glob. Biogeochem. Cycles 26 (1), http://dx.doi.org/10.1029/2010GB003952.

Bricaud, A., Claustre, H., Ras, J., Oubelkheir, K., 2004. Natural variability of phytoplanktonic absorption in oceanic waters: Influence of the size structure of algal populations. J. Geophys. Res. 109 (C11), http://dx.doi.org/10.1029/2004JC002419.

Bricaud, A., Morel, A., Babin, M., Allali, K., Claustre, H., 1998a. Absorption coefficients of particulate matter and chlorophyll a concentrations at time series station OLIPAC. http://dx.doi.org/10.1594/PANGAEA.739879.

Bricaud, A., Morel, A., Babin, M., Allali, K., Claustre, H., 1998b. Variations of light absorption by suspended particles with chlorophyll a concentration in oceanic (case 1) waters: Analysis and implications for bio-optical models. J. Geophys. Res.: Oceans 103 (C13), 31033–31044. http://dx.doi.org/10.1029/98JC02712.

Bricaud, A., Morel, A., Prieur, L., 1981. Absorption by dissolved organic matter of the sea (yellow substance) in the UV and visible domains1. Limnol. Oceanogr. 26 (1), 43–53. http://dx.doi.org/10.4319/lo.1981.26.1.0043.

Cael, B.B., Bisson, K., Boss, E., Dutkiewicz, S., Henson, S., 2023. Global climate-change trends detected in indicators of ocean ecology. Nature 619 (7970), 551–554. http://dx.doi.org/10.1038/s41586-023-06321-z.

Clementson, L.A., Parslow, J.S., Turnbull, A.R., McKenzie, D.C., Rathbone, C.E., 2001. Optical properties of waters in the Australasian sector of the Southern Ocean. J. Geophys. Res.: Oceans 106 (C12), 31611–31625. http://dx.doi.org/10.1029/2000JC000359.

Coble, P.G., 2007. Marine optical biogeochemistry: The chemistry of ocean color. Chem. Rev. 107 (2), 402–418. http://dx.doi.org/10.1021/cr050350+.

Dall'Olmo, G., Boss, E., Behrenfeld, M.J., Westberry, T.K., 2012. Particulate optical scattering coefficients along an Atlantic Meridional Transect. Opt. Express 20 (19), 21532. http://dx.doi.org/10.1364/OE.20.021532.

Dall'Olmo, G., Boss, E., Behrenfeld, M.J., Westberry, T.K., Courties, C., Prieur, L., Pujo-Pay, M., Hardman-Mountford, N., Moutin, T., 2011. Inferring phytoplankton carbon and eco-physiological rates from diel cycles of spectral particulate beam-attenuation coefficient. Biogeosciences 8 (11), 3423–3439. http://dx.doi.org/10.5194/bg-8-3423-2011.

Dall'Olmo, G., Brewin, R.J.W., Nencioli, F., Organelli, E., Lefering, I., McKee, D., Röttgers, R., Mitchell, C., Boss, E., Bricaud, A., Tilstone, G., 2017. Determination of the absorption coefficient of chromophoric dissolved organic matter from underway spectrophotometry. Opt. Express 25 (24), A1079. http://dx.doi.org/10.1364/oe.25.0a1079.

Dall'Olmo, G., Westberry, T.K., Behrenfeld, M.J., Boss, E., Slade, W.H., 2009. Significant contribution of large particles to optical backscattering in the open ocean. Biogeosciences 6 (6), 947–967. http://dx.doi.org/10.5194/bg-6-947-2009.

Defoin-Platel, M., Chami, M., 2007. How ambiguous is the inverse problem of ocean color in coastal waters? J. Geophys. Res. 112 (C3), http://dx.doi.org/10.1029/2006JC003847.

Devred, E., Perry, T., Massicotte, P., 2022. Seasonal and decadal variations in absorption properties of phytoplankton and non-algal particulate matter in three oceanic regimes of the Northwest Atlantic. Front. Mar. Sci. 9, http://dx.doi.org/10.3389/fmars.2022.932184.

Devred, E., Sathyendranath, S., Stuart, V., Maass, H., Ulloa, O., Platt, T., 2006. A two-component model of phytoplankton absorption in the open ocean: Theory and applications. J. Geophys. Res. 111 (C3), http://dx.doi.org/10.1029/2005JC002880.

Devred, E., Sathyendranath, S., Stuart, V., Platt, T., 2011. A three component classification of phytoplankton absorption spectra: Application to ocean-color data. Remote Sens. Environ. 115 (9), 2255–2266. http://dx.doi.org/10.1016/j.rse.2011.04.025.

D'Sa, E.J., Miller, R.L., Del Castillo, C., 2006. Bio-optical properties and ocean color algorithms for coastal waters influenced by the Mississippi River during a cold front. Appl. Opt. 45 (28), 7410. http://dx.doi.org/10.1364/AO.45.007410.

Dupouy, C., 2003. Microbial absorption and backscattering coefficients from in situ and POLDER satellite data during an El Niño–Southern Oscillation cold phase in the equatorial Pacific (180°). J. Geophys. Res. 108 (C12), http://dx.doi.org/10.1029/2001JC001298.

Dutkiewicz, S., Hickman, A.E., Jahn, O., Gregg, W.W., Mouw, C.B., Follows, M.J., 2015. Capturing optically important constituents and properties in a marine biogeochemical and ecosystem model. Biogeosciences 12 (14), 4447–4481. http://dx.doi.org/10.5194/bg-12-4447-2015.

Dutkiewicz, S., Hickman, A.E., Jahn, O., Henson, S., Beaulieu, C., Monier, E., 2019. Ocean colour signature of climate change. Nature Commun. 10 (1), http://dx.doi.org/10.1038/s41467-019-08457-x.

Ferreira, A., Ciotti, Á.M., Garcia, C.A.E., 2018. Bio-optical characterization of the northern Antarctic Peninsula waters: Absorption budget and insights on particulate backscattering. Deep Sea Res. II: Top. Stud. Oceanogr. 149, 138–149. http://dx.doi.org/10.1016/j.dsr2.2017.09.007.

Garaba, S.P., Wernand, M.R., Zielinski, O., 2011. Radiance, irradiance, and remote sensing reflectance during the North Sea Coast Harmful Algal Bloom (NORCOHAB II) HEINCKE cruise HE302. http://dx.doi.org/10.1594/PANGAEA.759690.

Golbol, M., Vellucci, V., Antoine, D., 2000. BOUSSOLE. http://dx.doi.org/10.18142/1, URL https://campagnes.flotteoceanographique.fr/series/1/.

Gonçalves-Araujo, R., Wiegmann, S., Bracher, A., 2018a. Absorption coefficient spectra of non-algal particles during POLARSTERN cruise ARK-XXVI/3 (PS78, TRANSARC). http://dx.doi.org/10.1594/PANGAEA.885245.

Gonçalves-Araujo, R., Wiegmann, S., Bracher, A., 2018b. Phytoplankton absorption coefficient spectra during POLARSTERN cruise ARK-XXVI/3 (PS78, TRANSARC). http://dx.doi.org/10.1594/PANGAEA.885246.

Gordon, H.R., Brown, O.B., Evans, R.H., Brown, J.W., Smith, R.C., Baker, K.S., Clark, D.K., 1988. A semianalytic radiance model of ocean color. J. Geophys. Res. 93 (D9), 10909. http://dx.doi.org/10.1029/JD093iD09p10909.

Graban, S., Dall'Olmo, G., Goult, S., Sauzède, R., 2020. Accurate deep-learning estimation of chlorophyll-a concentration from the spectral particulate beam-attenuation coefficient. Opt. Express 28 (16), 24214. http://dx.doi.org/10.1364/OE.397863.

Hammond, M.L., Beaulieu, C., Henson, S.A., Sahu, S.K., 2020. Regional surface chlorophyll trends and uncertainties in the global ocean. Sci. Rep. 10 (1), http://dx.doi.org/10.1038/s41598-020-72073-9.

Hoepffner, N., Sathyendranath, S., 1991. Effect of pigment composition on absorption properties of phytoplankton. Mar. Ecol. Progr. Ser. 73, 11–23. http://dx.doi.org/10.3354/meps073011.

Hu, C., Lee, Z., Walsh, J.J., 2006. Ocean color reveals phase shift between marine plants and yellow substance. IEEE Geosci. Remote Sens. Lett. 3 (2), 262–266. http://dx.doi.org/10.1109/LGRS.2005.862527.

Huot, Y., Antoine, D., 2016. Remote sensing reflectance anomalies in the ocean. Remote Sens. Environ. 184, 101–111. http://dx.doi.org/10.1016/j.rse.2016.06.002.

Huot, Y., Morel, A., Twardowski, M.S., Stramski, D., Reynolds, R.A., 2008. Particle optical backscattering along a chlorophyll gradient in the upper layer of the eastern South Pacific Ocean. Biogeosciences 5 (2), 495–507. http://dx.doi.org/10.5194/bg-5-495-2008.

IMOS, 2022. IMOS - SRS - ocean colour - bio optical database of Australian waters. URL https://catalogue-imos.aodn.org.au/geonetwork/srv/eng/catalog.search#/metadata/97b9fe73-ee44-437f-b2ae-5b8613f81042.

Jackson, T., Sathyendranath, S., Mélin, F., 2017. An improved optical classification scheme for the Ocean Colour Essential Climate Variable and its applications. Remote Sens. Environ. 203, 152–161. http://dx.doi.org/10.1016/j.rse.2017.03.036.

Jeffrey, S.W., Wright, S.W., Zapata, M., 2011. Microalgal classes and their signature pigments. In: Roy, S., Llewellyn, C.A., Egeland, E.S., Johnsen, G. (Eds.), Phytoplankton Pigments. Cambridge University Press, pp. 3–77. http://dx.doi.org/10.1017/CBO9780511732263.004.

Johnson, R., Strutton, P.G., Wright, S.W., McMinn, A., Meiners, K.M., 2013. Three improved satellite chlorophyll algorithms for the Southern Ocean. J. Geophys. Res.: Oceans 118 (7), 3694–3703. http://dx.doi.org/10.1002/jgrc.20270.

Kheireddine, M., Antoine, D., 2014. Diel variability of the beam attenuation and backscattering coefficients in the northwestern Mediterranean Sea (BOUSSOLE site). J. Geophys. Res.: Oceans 119 (8), 5465–5482. http://dx.doi.org/10.1002/2014JC010007.

Kheireddine, M., Brewin, R.J.W., Ouhssain, M., Jones, B.H., 2021. Particulate scattering and backscattering in relation to the nature of particles in the red sea. J. Geophys. Res.: Oceans 126 (4), http://dx.doi.org/10.1029/2020JC016610.

Kheireddine, M., Ouhssain, M., Calleja, M.L., Morán, X.A.G., Sarma, Y.V.B., Tiwari, S.P., Jones, B.H., 2018a. Characterization of light absorption by chromophoric dissolved organic matter (CDOM) in the upper layer of the Red Sea. Deep Sea Res. Part I: Oceanogr. Res. Pap. 133, 72–84. http://dx.doi.org/10.1016/j.dsr.2018.02.001.

Kheireddine, M., Ouhssain, M., Organelli, E., Bricaud, A., Jones, B.H., 2018b. Light absorption by suspended particles in the red sea: Effect of phytoplankton community size structure and pigment composition. J. Geophys. Res.: Oceans 123 (2), 902–921. http://dx.doi.org/10.1002/2017JC013279.

Kostadinov, T.S., Siegel, D.A., Maritorena, S., 2009. Retrieval of the particle size distribution from satellite ocean color observations. J. Geophys. Res. 114 (C9), http://dx.doi.org/10.1029/2009JC005303.

Kramer, S.J., Siegel, D.A., Maritorena, S., Catlett, D., 2021. Global surface ocean HPLC phytoplankton pigments and hyperspectral remote sensing reflectance. http://dx.doi.org/10.1594/PANGAEA.937536.

Krug, L.A., Platt, T., Sathyendranath, S., Barbosa, A.B., 2017. Ocean surface partitioning strategies using ocean colour remote Sensing: A review. Prog. Oceanogr. 155, 41–53. http://dx.doi.org/10.1016/j.pocean.2017.05.013.

Lee, Z., Carder, K.L., Arnone, R.A., 2002. Deriving inherent optical properties from water color: a multiband quasi-analytical algorithm for optically deep waters. Appl. Opt. 41 (27), 5755. http://dx.doi.org/10.1364/AO.41.005755.

Lee, Z., Carder, K.L., Hawes, S.K., Steward, R.G., Peacock, T.G., Davis, C.O., 1994. Model for the interpretation of hyperspectral remote-sensing reflectance. Appl. Opt. 33 (24), 5721. http://dx.doi.org/10.1364/AO.33.005721.

Lee, Z.P., Du, K., Voss, K.J., Zibordi, G., Lubac, B., Arnone, R., Weidemann, A., 2011. An inherent-optical-property-centered approach to correct the angular effects in water-leaving radiance. Appl. Opt. 50 (19), 3155. http://dx.doi.org/10.1364/AO.50.003155.

Lee, Z., Hu, C., Shang, S., Du, K., Lewis, M., Arnone, R., Brewin, R., 2013. Penetration of UV-visible solar radiation in the global oceans: Insights from ocean color remote sensing. J. Geophys. Res.: Oceans 118 (9), 4241–4255. http://dx.doi.org/10.1002/jgrc.20308.

Lee, Z., Shang, S., Zhang, S., Wu, J., Wei, G., Wu, X., 2020. Impact of temporal variation of chlorophyll-specific absorption on phytoplankton phenology observed from ocean color satellite: A numerical experiment. J. Geophys. Res.: Oceans 125 (12), http://dx.doi.org/10.1029/2020JC016382.

Lee, Z., Wei, J., Voss, K., Lewis, M., Bricaud, A., Huot, Y., 2015. Hyperspectral absorption coefficient of "pure" seawater in the range of 350-550 nm inverted from remote sensing reflectance. Appl. Opt. 54 (3), 546. http://dx.doi.org/10.1364/AO.54.000546.

Leonelli, F.E., Bellacicco, M., Pitarch, J., Organelli, E., Nardelli, B.B., de Toma, V., Cammarota, C., Marullo, S., Santoleri, R., 2022. Ultra-oligotrophic waters expansion in the north atlantic subtropical gyre revealed by 21 years of satellite observations. Geophys. Res. Lett. 49 (21), http://dx.doi.org/10.1029/2021GL096965.

Lewis, K.M., Arrigo, K.R., 2020. Ocean color algorithms for estimating chlorophyll a, CDOM absorption, and particle backscattering in the arctic ocean. J. Geophys. Res.: Oceans 125 (6), http://dx.doi.org/10.1029/2019JC015706.

Lewis, K.M., van Dijken, G.L., Arrigo, K.R., 2020. Changes in phytoplankton concentration now drive increased Arctic Ocean primary production. Science 369 (6500), 198–202. http://dx.doi.org/10.1126/science.aay8380.

Lewis, K.M., Mitchell, B.G., van Dijken, G.L., Arrigo, K.R., 2016. Regional chlorophyll a algorithms in the Arctic Ocean and their effect on satellite-derived primary production estimates. Deep Sea Res. II: Top. Stud. Oceanogr. 130, 14–27. http://dx.doi.org/10.1016/j.dsr2.2016.04.020.

Li, M., Shen, F., Sun, X., 2021. 2019–2020 Australian bushfire air particulate pollution and impact on the South Pacific Ocean. Sci. Rep. 11 (1), http://dx.doi.org/10.1038/s41598-021-91547-y.

Li, L., Stramski, D., Reynolds, R.A., 2016. Effects of inelastic radiative processes on the determination of water-leaving spectral radiance from extrapolation of underwater near-surface measurements. Appl. Opt. 55 (25), 7050. http://dx.doi.org/10.1364/AO.55.007050.

Litchman, E., Pinto, P.d., Edwards, K.F., Klausmeier, C.A., Kremer, C.T., Thomas, M.K., 2015. Global biogeochemical impacts of phytoplankton: a trait-based perspective. In: Austin, A. (Ed.), J. Ecol. 103 (6), 1384–1396. http://dx.doi.org/10.1111/1365-2745.12438.

Liu, Y., Boss, E., Chase, A.P., Xi, H., Zhang, X., Röttgers, R., Pan, Y., Bracher, A., 2018a. Phytoplankton pigment concentration measured by HPLC during POLARSTERN cruise PS107. http://dx.doi.org/10.1594/PANGAEA.894860.

Liu, Y., Boss, E., Chase, A.P., Xi, H., Zhang, X., Röttgers, R., Pan, Y., Bracher, A., 2018b. Phytoplankton pigment concentration measured by HPLC during POLARSTERN cruise PS93.2. http://dx.doi.org/10.1594/PANGAEA.894872.

Liu, Y., Boss, E., Chase, A.P., Xi, H., Zhang, X., Röttgers, R., Pan, Y., Bracher, A., 2018c. Phytoplankton pigment concentration measured by HPLC during POLARSTERN cruise PS99. http://dx.doi.org/10.1594/PANGAEA.894874.

Liu, Y., Hellmann, S., Wiegmann, S., Bracher, A., 2019a. Phytoplankton pigment concentrations measured by HPLC during POLARSTERN cruise PS99.1. http://dx.doi.org/10.1594/PANGAEA.905502.

Liu, Y., Wiegmann, S., Bracher, A., 2019b. Spectrophotometric measurements of absorption coefficients and optical density by total particles, phytoplankton and non-algal particles during POLARSTERN cruise PS107. http://dx.doi.org/10.1594/PANGAEA.907419.

Liu, Y., Wiegmann, S., Bracher, A., 2019c. Spectrophotometric measurements of absorption coefficients and optical density by total particles, phytoplankton and non-algal particles during POLARSTERN cruise PS99. http://dx.doi.org/10.1594/PANGAEA.907648.

Lohrenz, S.E., Weidemann, A.D., Tuel, M., 2003. Phytoplankton spectral absorption as influenced by community size structure and pigment composition. J. Plankton Res. 25 (1), 35–61. http://dx.doi.org/10.1093/plankt/25.1.35.

Loisel, H., Nicolas, J.-M., Sciandra, A., Stramski, D., Poteau, A., 2006. Spectral dependency of optical backscattering by marine particles from satellite remote sensing of the global ocean. J. Geophys. Res. 111 (C9), http://dx.doi.org/10.1029/2005JC003367.

López-Urrutia, Á., Morán, X.A.G., 2015. Temperature affects the size-structure of phytoplankton communities in the ocean. Limnol. Oceanogr. 60 (3), 733–738. http://dx.doi.org/10.1002/lno.10049.

Maniaci, G., Brewin, R.J.W., Sathyendranath, S., 2022. Concentration and distribution of phytoplankton nitrogen and carbon in the Northwest Atlantic and Indian Ocean: A simple model with applications in satellite remote sensing. Front. Mar. Sci. 9, http://dx.doi.org/10.3389/fmars.2022.1035399.

Marañón, E., Cermeño, P., Latasa, M., Tadonléké, R.D., 2015. Resource supply alone explains the variability of marine phytoplankton size structure. Limnol. Oceanogr. 60 (5), 1848–1854. http://dx.doi.org/10.1002/lno.10138.

Martinez-Vicente, V., Tilstone, G.H., Sathyendranath, S., Miller, P.I., Groom, S.B., 2012. Contributions of phytoplankton and bacteria to the optical backscattering coefficient over the Mid-Atlantic Ridge. Mar. Ecol. Progr. Ser. 445, 37–51. http://dx.doi.org/10.3354/meps09388.

McClain, C.R., 2009. A decade of satellite ocean color observations. Ann. Rev. Mar. Sci. 1 (1), 19–42. http://dx.doi.org/10.1146/annurev.marine.010908.163650.

Mélin, F., Vantrepotte, V., Chuprin, A., Grant, M., Jackson, T., Sathyendranath, S., 2017. Assessing the fitness-for-purpose of satellite multi-mission ocean color climate data records: A protocol applied to OC-CCI chlorophyll- a data. Remote Sens. Environ. 203, 139–151. http://dx.doi.org/10.1016/j.rse.2017.03.039.

Minnett, P.J., Alvera-Azcárate, A., Chin, T.M., Corlett, G.K., Gentemann, C.L., Karagali, I., Li, X., Marsouin, A., Marullo, S., Maturi, E., Santoleri, R., Picart, S.S., Steele, M., Vazquez-Cuervo, J., 2019. Half a century of satellite remote sensing of sea-surface temperature. Remote Sens. Environ. 233, 111366. http://dx.doi.org/10.1016/j.rse.2019.111366.

Montégut, C.d., Madec, G., Fischer, A.S., Lazar, A., Iudicone, D., 2004. Mixed layer depth over the global ocean: An examination of profile data and a profile-based climatology. J. Geophys. Res. 109 (C12), http://dx.doi.org/10.1029/2004JC002378.

Morel, A., 1988. Optical modeling of the upper ocean in relation to its biogenous matter content (case I waters). J. Geophys. Res.: Oceans 93 (C9), 10749–10768. http://dx.doi.org/10.1029/JC093iC09p10749.

Morel, A., 2009. Are the empirical relationships describing the bio-optical properties of case 1 waters consistent and internally compatible? J. Geophys. Res. 114 (C1), http://dx.doi.org/10.1029/2008JC004803.

Morel, A., Antoine, D., Gentili, B., 2002. Bidirectional reflectance of oceanic waters: accounting for Raman emission and varying particle scattering phase function. Appl. Opt. 41 (30), 6289. http://dx.doi.org/10.1364/AO.41.006289.

Morel, A., Gentili, B., 2009. A simple band ratio technique to quantify the colored dissolved and detrital organic material from ocean color remotely sensed data. Remote Sens. Environ. 113 (5), 998–1011. http://dx.doi.org/10.1016/j.rse.2009.01.008.

Morel, A., Maritorena, S., 2001. Bio-optical properties of oceanic waters: A reappraisal. J. Geophys. Res.: Oceans 106 (C4), 7163–7180. http://dx.doi.org/10.1029/2000JC000319.

Morel, A., Prieur, L., 1977. Analysis of variations in ocean color1. Limnol. Oceanogr. 22 (4), 709–722. http://dx.doi.org/10.4319/lo.1977.22.4.0709.

Moutin, T., Claustre, H., 2013. Pigments measured on water bottle samples during L'Atalante cruise OLIPAC. http://dx.doi.org/10.1594/PANGAEA.804990.

Naik, P., D'Sa, E.J., do R. Gomes, H., Goés, J.I., Mouw, C.B., 2013. Light absorption properties of southeastern Bering Sea waters: Analysis, parameterization and implications for remote sensing. Remote Sens. Environ. 134, 120–134. http://dx.doi.org/10.1016/j.rse.2013.03.004.

Nelson, N.B., Siegel, D.A., 2013. The global distribution and dynamics of chromophoric dissolved organic matter. Ann. Rev. Mar. Sci. 5 (1), 447–476. http://dx.doi.org/10.1146/annurev-marine-120710-100751.

Nelson, N.B., Siegel, D.A., Michaels, A.F., 1998. Seasonal dynamics of colored dissolved material in the Sargasso Sea. Deep Sea Res. Part I: Oceanogr. Res. Pap. 45 (6), 931–957. http://dx.doi.org/10.1016/S0967-0637(97)00106-4.

Neukermans, G., Reynolds, R.A., Stramski, D., 2016. Optical classification and characterization of marine particle assemblages within the western Arctic Ocean. Limnol. Oceanogr. 61 (4), 1472–1494. http://dx.doi.org/10.1002/lno.10316.

O'Reilly, J.E., Maritorena, S., Mitchell, B.G., Siegel, D.A., Carder, K.L., Garver, S.A., Kahru, M., McClain, C., 1998. Ocean color chlorophyll algorithms for SeaWiFS. J. Geophys. Res.: Oceans 103 (C11), 24937–24953. http://dx.doi.org/10.1029/98JC02160.

O'Reilly, J.E., Werdell, P.J., 2019. Chlorophyll algorithms for ocean color sensors - OC4, OC5 & OC6. Remote Sens. Environ. 229, 32–47. http://dx.doi.org/10.1016/j.rse.2019.04.021.

Organelli, E., Bricaud, A., Antoine, D., Matsuoka, A., 2014. Seasonal dynamics of light absorption by chromophoric dissolved organic matter (CDOM) in the NW Mediterranean Sea (BOUSSOLE site). Deep Sea Res. Part I: Oceanogr. Res. Pap. 91, 72–85. http://dx.doi.org/10.1016/j.dsr.2014.05.003.

Organelli, E., Claustre, H., 2019. Small phytoplankton shapes colored dissolved organic matter dynamics in the north atlantic subtropical gyre. Geophys. Res. Lett. 46 (21), 12183–12191. http://dx.doi.org/10.1029/2019GL084699.

Organelli, E., Dall'Olmo, G., Brewin, R.J.W., Tarran, G.A., Boss, E., Bricaud, A., 2018. The open-ocean missing backscattering is in the structural complexity of particles. Nature Commun. 9 (1), http://dx.doi.org/10.1038/s41467-018-07814-6.

Organelli, E., Nuccio, C., Lazzara, L., Uitz, J., Bricaud, A., Massi, L., 2017. On the discrimination of multiple phytoplankton groups from light absorption spectra of assemblages with mixed taxonomic composition and variable light conditions. Appl. Opt. 56 (14), 3952. http://dx.doi.org/10.1364/AO.56.003952.

Peeken, I., Murawski, S., 2016. Chlorophyll a measured on water bottle samples using HPLC during POLARSTERN cruise ARK-XXVI/3 (TRANSARC). http://dx.doi.org/10.1594/PANGAEA.867473.

Peeken, I., Nachtigall, K., 2014. Phytoplankton pigments measured on water bottle samples during POLARSTERN cruise ANT-XXVI/3. http://dx.doi.org/10.1594/PANGAEA.869826.

Pereira, E.S., Garcia, C.A.E., 2018. Evaluation of satellite-derived MODIS chlorophyll algorithms in the northern Antarctic Peninsula. Deep Sea Res. II: Top. Stud. Oceanogr. 149, 124–137. http://dx.doi.org/10.1016/j.dsr2.2017.12.018.

Pérez, G.L., Galí, M., Royer, S.-J., Sarmento, H., Gasol, J.M., Marrasé, C., Simó, R., 2016. Bio-optical characterization of offshore NW Mediterranean waters: CDOM contribution to the absorption budget and diffuse attenuation of downwelling irradiance. Deep Sea Res. Part I: Oceanogr. Res. Pap. 114, 111–127. http://dx.doi.org/10.1016/j.dsr.2016.05.011.

Pitarch, J., Volpe, G., Colella, S., Santoleri, R., Brando, V., 2016. Absorption correction and phase function shape effects on the closure of apparent optical properties. Appl. Opt. 55 (30), 8618. http://dx.doi.org/10.1364/AO.55.008618.

Pope, R.M., Fry, E.S., 1997. Absorption spectrum (380–700 nm) of pure water. II. Integrating cavity measurements. Appl. Opt. 36 (33), 8710. http://dx.doi.org/10.1364/AO.36.008710.

Poulin, C., Antoine, D., Huot, Y., 2018. Diurnal variations of the optical properties of phytoplankton in a laboratory experiment and their implication for using inherent optical properties to measure biomass. Opt. Express 26 (2), 711. http://dx.doi.org/10.1364/OE.26.000711.

Prieur, L., Sathyendranath, S., 1981. An optical classification of coastal and oceanic waters based on the specific spectral absorption curves of phytoplankton pigments, dissolved organic matter, and other particulate materials1. Limnol. Oceanogr. 26 (4), 671–689. http://dx.doi.org/10.4319/lo.1981.26.4.0671.

Reynolds, R.A., Stramski, D., 2019. Optical characterization of marine phytoplankton assemblages within surface waters of the western Arctic Ocean. Limnol. Oceanogr. 64 (6), 2478–2496. http://dx.doi.org/10.1002/lno.11199.

Reynolds, R.A., Stramski, D., Mitchell, B.G., 2001. A chlorophyll-dependent semi-analytical reflectance model derived from field measurements of absorption and backscattering coefficients within the Southern Ocean. J. Geophys. Res.: Oceans 106 (C4), 7125–7138. http://dx.doi.org/10.1029/1999JC000311.

Richardson, A.J., Schoeman, D.S., 2004. Climate impact on plankton ecosystems in the northeast atlantic. Science 305 (5690), 1609–1612. http://dx.doi.org/10.1126/science.1100958.

Robinson, C.M., Huot, Y., Schuback, N., Ryan-Keogh, T.J., Thomalla, S.J., Antoine, D., 2021. High latitude Southern Ocean phytoplankton have distinctive bio-optical properties. Opt. Express 29 (14), 21084. http://dx.doi.org/10.1364/OE.426737.

Roesler, C.S., Perry, M.J., Carder, K.L., 1989. Modeling in situ phytoplankton absorption from total absorption spectra in productive inland marine waters. Limnol. Oceanogr. 34 (8), 1510–1523. http://dx.doi.org/10.4319/lo.1989.34.8.1510.

Roesler, C., Uitz, J., Claustre, H., Boss, E., Xing, X., Organelli, E., Briggs, N., Bricaud, A., Schmechtig, C., Poteau, A., D'Ortenzio, F., Ras, J., Drapeau, S., Haëntjens, N., Barbieux, M., 2017. Recommendations for obtaining unbiased chlorophyll estimates from in situ chlorophyll fluorometers: A global analysis of WET Labs ECO sensors. Limnol. Oceanogr.: Methods 15 (6), 572–585. http://dx.doi.org/10.1002/lom3.10185.

Röttgers, R., Bi, S., Burmester, H., Heymann, K., Hieronymi, M., Krasemann, H., Schönfeld, W., 2023. Water inherent optical properties and concentrations of water constituents from the German Bight and adjacent regions. http://dx.doi.org/10.1594/PANGAEA.950774.

Röttgers, R., McKee, D., Utschig, C., 2014. Temperature and salinity correction coefficients for light absorption by water in the visible to infrared spectral region. Opt. Express 22 (21), 25093. http://dx.doi.org/10.1364/OE.22.025093.

Rudorff, N.d., Frouin, R., Kampel, M., Goyens, C., Meriaux, X., Schieber, B., Mitchell, B.G., 2014. Ocean-color radiometry across the Southern Atlantic and Southeastern Pacific: Accuracy and remote sensing implications. Remote Sens. Environ. 149, 13–32. http://dx.doi.org/10.1016/j.rse.2014.03.029.

Santoleri, R., Volpe, G., Marullo, S., Nardelli, B.B., 2008. Open waters optical remote sensing of the mediterranean sea. In: Barale, V., Gade, M. (Eds.), Remote Sensing of the European Seas. Springer Netherlands, pp. 103–116. http://dx.doi.org/10.1007/978-1-4020-6772-3_8.

Sathyendranath, S., Brewin, R., Brockmann, C., Brotas, V., Calton, B., Chuprin, A., Cipollini, P., Couto, A., Dingle, J., Doerffer, R., Donlon, C., Dowell, M., Farman, A., Grant, M., Groom, S., Horseman, A., Jackson, T., Krasemann, H., Lavender, S., Martinez-Vicente, V., Mazeran, C., Mélin, F., Moore, T., Müller, D., Regner, P., Roy, S., Steele, C., Steinmetz, F., Swinton, J., Taberner, M., Thompson, A., Valente, A., Zühlke, M., Brando, V., Feng, H., Feldman, G., Franz, B., Frouin, R., Gould, R., Hooker, S., Kahru, M., Kratzer, S., Mitchell, B., Muller-Karger, F., Sosik, H., Voss, K., Werdell, J., Platt, T., 2019. An ocean-colour time series for use in climate studies: The experience of the ocean-colour climate change initiative (OC-CCI). Sensors 19 (19), 4285. http://dx.doi.org/10.3390/s19194285.

Sathyendranath, S., Brewin, R.J.W., Jackson, T., Mélin, F., Platt, T., 2017. Ocean-colour products for climate-change studies: What are their ideal characteristics? Remote Sens. Environ. 203, 125–138. http://dx.doi.org/10.1016/j.rse.2017.04.017.

Sathyendranath, S., Bukata, R.P., Arnone, R., Dowell, M.D., Davis, C.O., Babin, M., Berthon, J.-F., Kopelevich, O.V., Campbell, J.W., 2000. Colour of case 2 waters. In: Sathyendranath, S. (Ed.), Remote Sensing of Ocean Colour in Coastal, and Other Optically-Complex, WatersEdited. Reports of the International Ocean-Colour Coordinating Group, No. 15, IOCCG, Dartmouth, Canada., pp. 23–46.

Sathyendranath, S., Cota, G., Stuart, V., Maass, H., Platt, T., 2001. Remote sensing of phytoplankton pigments: A comparison of empirical and theoretical approaches. Int. J. Remote Sens. 22 (2–3), 249–273. http://dx.doi.org/10.1080/014311601449925.

Sathyendranath, S., Jackson, T., Brockmann, C., Brotas, V., Calton, B., Chuprin, A., Clements, O., Cipollini, P., Danne, O., Dingle, J., Donlon, C., Grant, M., Groom, S., Krasemann, H., Lavender, S., Mazeran, C., Mélin, F., Müller, D., Steinmetz, F., Valente, A., Zühlke, M., Feldman, G., Franz, B., Frouin, R., Werdell, J., Platt, T., 2021. ESA ocean colour climate change initiative (Ocean_Colour_cci): Version 5.0 data. http://dx.doi.org/10.5285/1dbe7a109c0244aaad713e078fd3059a.

Sathyendranath, S., Platt, T., 1997. Analytic model of ocean color. Appl. Opt. 36 (12), 2620. http://dx.doi.org/10.1364/AO.36.002620.

Sathyendranath, S., Platt, T., 1998. Ocean-color model incorporating transspectral processes. Appl. Opt. 37 (12), 2216. http://dx.doi.org/10.1364/ao.37.002216.

Sathyendranath, S., Stuart, V., Nair, A., Oka, K., Nakane, T., Bouman, H., Forget, M.H., Maass, H., Platt, T., 2009. Carbon-to-chlorophyll ratio and growth rate of phytoplankton in the sea. Mar. Ecol. Progr. Ser. 383, 73–84. http://dx.doi.org/10.3354/meps07998.

Sathyendranath, S., Watts, L., Devred, E., Platt, T., Caverhill, C., Maass, H., 2004. Discrimination of diatoms from other phytoplankton using ocean-colour data. Mar. Ecol. Progr. Ser. 272, 59–68. http://dx.doi.org/10.3354/meps272059.

Sieburth, J.M., Smetacek, V., Lenz, J., 1978. Pelagic ecosystem structure: Heterotrophic compartments of the plankton and their relationship to plankton size fractions 1. Limnol. Oceanogr. 23 (6), 1256–1263. http://dx.doi.org/10.4319/lo.1978.23.6.1256.

Siegel, D.A., Maritorena, S., Nelson, N.B., Hansell, D.A., Lorenzi-Kayser, M., 2002. Global distribution and dynamics of colored dissolved and detrital organic materials. J. Geophys. Res.: Oceans 107 (C12), 21–1–21–14. http://dx.doi.org/10.1029/2001JC000965.

Slade, W.H., Boss, E., 2015. Spectral attenuation and backscattering as indicators of average particle size. Appl. Opt. 54 (24), 7264. http://dx.doi.org/10.1364/AO.54.007264.

Soja-Woźniak, M., Laiolo, L., Baird, M.E., Matear, R., Clementson, L., Schroeder, T., Doblin, M.A., Suthers, I.M., 2020. Effect of phytoplankton community size structure on remote-sensing reflectance and chlorophyll a products. J. Mar. Syst. 211, 103400. http://dx.doi.org/10.1016/j.jmarsys.2020.103400.

Soppa, M.A., Dinter, T., Taylor, B.B., Bracher, A., 2013a. Particulate absorption during POLARSTERN cruise ANT-XXVI/3. http://dx.doi.org/10.1594/PANGAEA.819611.

Soppa, M.A., Dinter, T., Taylor, B.B., Bracher, A., 2013b. Particulate absorption during POLARSTERN cruise ANT-XXVIII/3. http://dx.doi.org/10.1594/PANGAEA.819613.

Soppa, M.A., Dinter, T., Taylor, B.B., Bracher, A., 2013c. Phytoplankton absorption during POLARSTERN cruise ANT-XXVI/3. http://dx.doi.org/10.1594/PANGAEA.819612.

Soppa, M.A., Dinter, T., Taylor, B.B., Bracher, A., 2013d. Phytoplankton absorption during POLARSTERN cruise ANT-XXVIII/3. http://dx.doi.org/10.1594/PANGAEA.819614.

Stemmann, L., Boss, E., 2012. Plankton and particle size and packaging: From determining optical properties to driving the biological pump. Ann. Rev. Mar. Sci. 4 (1), 263–290. http://dx.doi.org/10.1146/annurev-marine-120710-100853.

Stock, A., Subramaniam, A., 2022. Iterative spatial leave-one-out cross-validation and gap-filling based data augmentation for supervised learning applications in marine remote sensing. GISci. Remote Sens. 59 (1), 1281–1300. http://dx.doi.org/10.1080/15481603.2022.2107113.

Stramski, D., Boss, E., Bogucki, D., Voss, K.J., 2004. The role of seawater constituents in light backscattering in the ocean. Prog. Oceanogr. 61 (1), 27–56. http://dx.doi.org/10.1016/j.pocean.2004.07.001.

Stramski, D., Bricaud, A., Morel, A., 2001. Modeling the inherent optical properties of the ocean based on the detailed composition of the planktonic community. Appl. Opt. 40 (18), 2929. http://dx.doi.org/10.1364/AO.40.002929.

Stramski, D., Kiefer, D.A., 1990. Optical properties of marine bacteria. In: Spinrad, R.W. (Ed.), SPIE Proceedings. SPIE 1302, http://dx.doi.org/10.1117/12.21450.

Stramski, D., Mobley, C.D., 1997. Effects of microbial particles on oceanic optics: A database of single-particle optical properties. Limnol. Oceanogr. 42 (3), 538–549. http://dx.doi.org/10.4319/lo.1997.42.3.0538.

Stramski, D., Reynolds, R.A., Babin, M., Kaczmarek, S., Lewis, M.R., Röttgers, R., Sciandra, A., Stramska, M., Twardowski, M.S., Franz, B.A., Claustre, H., 2008a. Concentration of particulate organic carbon and optical properties in the eastern South Pacific and eastern Atlantic Oceans. http://dx.doi.org/10.1594/PANGAEA.759667.

Stramski, D., Reynolds, R.A., Babin, M., Kaczmarek, S., Lewis, M.R., Röttgers, R., Sciandra, A., Stramska, M., Twardowski, M.S., Franz, B.A., Claustre, H., 2008b. Relationships between the surface concentration of particulate organic carbon and optical properties in the eastern South Pacific and eastern Atlantic Oceans. Biogeosciences 5 (1), 171–201. http://dx.doi.org/10.5194/bg-5-171-2008.

Sun, X., Brewin, R.J.W., Sathyendranath, S., Dall'Olmo, G., Airs, R., Barlow, R., Bracher, A., Brotas, V., Kheireddine, M., Lamont, T., Marañón, E., Morán, X.A.G., Raitsos, D.E., Shen, F., Tilstone, G.H., 2023. Coupling ecological concepts with an ocean-colour model: Phytoplankton size structure. Remote Sens. Environ. 285, 113415. http://dx.doi.org/10.1016/j.rse.2022.113415.

Sun, X., Shen, F., Brewin, R.J.W., Li, M., Zhu, Q., 2022. Light absorption spectra of naturally mixed phytoplankton assemblages for retrieval of phytoplankton group composition in coastal oceans. Limnol. Oceanogr. 67 (4), 946–961. http://dx.doi.org/10.1002/lno.12047.

Szeto, M., Werdell, P.J., Moore, T.S., Campbell, J.W., 2011. Are the world's oceans optically different? J. Geophys. Res.: Oceans 116 (C7), http://dx.doi.org/10.1029/2011JC007230.

Taylor, B.B., Bracher, A., 2012a. Particulate absorption during SONNE cruise SO202/2 (TRANSBROM). http://dx.doi.org/10.1594/PANGAEA.804549.

Taylor, B.B., Bracher, A., 2012b. Phytoplankton absorption during SONNE cruise SO202/2 (TRANSBROM). http://dx.doi.org/10.1594/PANGAEA.804552.

Taylor, B.B., Bracher, A., 2017. Pigment concentrations measured in surface water during SONNE cruise SO202/2 (TRANSBROM). http://dx.doi.org/10.1594/PANGAEA.880235.

Taylor, B.B., Torrecilla, E., Bernhardt, A., Taylor, M.H., Peeken, I., Röttgers, R., Piera, J., Bracher, A., 2011a. Bio-optical provinces in the eastern Atlantic Ocean and their biogeographical relevance. Biogeosciences 8 (12), 3609–3629. http://dx.doi.org/10.5194/bg-8-3609-2011.

Taylor, B.B., Torrecilla, E., Bernhardt, A., Taylor, M.H., Peeken, I., Röttgers, R., Piera, J., Bracher, A., 2011b. Phytoplankton pigments, composition, hyperspectral light field data and biooptical properties during POLARSTERN cruise ANT-XXV/1. http://dx.doi.org/10.1594/PANGAEA.819099.

Terrats, L., Claustre, H., Cornec, M., Mangin, A., Neukermans, G., 2020. Detection of coccolithophore blooms with BioGeoChemical-argo floats. Geophys. Res. Lett. 47 (23), http://dx.doi.org/10.1029/2020GL090559.

Thomalla, S.J., Nicholson, S.-A., Ryan-Keogh, T.J., Smith, M.E., 2023. Widespread changes in Southern Ocean phytoplankton blooms linked to climate drivers. Nature Clim. Change 13 (9), 975–984. http://dx.doi.org/10.1038/s41558-023-01768-4.

Tonizzo, A., Twardowski, M., McLean, S., Voss, K., Lewis, M., Trees, C., 2016. Closure and uncertainty assessment for ocean color reflectance using measured volume scattering functions and reflective tube absorption coefficients with novel correction for scattering. Appl. Opt. 56 (1), 130. http://dx.doi.org/10.1364/AO.56.000130.

Twardowski, M.S., Donaghay, P.L., 2002. Photobleaching of aquatic dissolved materials: Absorption removal, spectral alteration, and their interrelationship. J. Geophys. Res.: Oceans 107 (C8), http://dx.doi.org/10.1029/1999JC000281.

Uitz, J., Huot, Y., Bruyant, F., Babin, M., Claustre, H., 2008. Relating phytoplankton photophysiological properties to community structure on large scales. Limnol. Oceanogr. 53 (2), 614–630. http://dx.doi.org/10.4319/lo.2008.53.2.0614.

Uitz, J., Stramski, D., Reynolds, R.A., Dubranna, J., 2015. Assessing phytoplankton community composition from hyperspectral measurements of phytoplankton absorption coefficient and remote-sensing reflectance in open-ocean environments. Remote Sens. Environ. 171, 58–74. http://dx.doi.org/10.1016/j.rse.2015.09.027.

Valente, A., Sathyendranath, S., Brotas, V., Groom, S., Grant, M., Jackson, T., Chuprin, A., Taberner, M., Airs, R., Antoine, D., Arnone, R., Balch, W.M., Barker, K., Barlow, R., Bélanger, S., Berthon, J.-F., Beşiktepe, Ş., Borsheim, Y., Bracher, A., Brando, V., Brewin, R.J.W., Canuti, E., Chavez, F.P., Cianca, A., Claustre, H., Clementson, L., Crout, R., Ferreira, A., Freeman, S., Frouin, R., García-Soto, C., Gibb, S.W., Goericke, R., Gould, R., Guillocheau, N., Hooker, S.B., Hu, C., Kahru, M., Kampel, M., Klein, H., Kratzer, S., Kudela, R., Ledesma, J., Lohrenz, S., Loisel, H., Mannino, A., Martinez-Vicente, V., Matrai, P., McKee, D., Mitchell, B.G., Moisan, T., Montes, E., Muller-Karger, F., Neeley, A., Novak, M., O'Dowd, L., Ondrusek, M., Platt, T., Poulton, A.J., Repecaud, M., Röttgers, R., Schroeder, T., Smyth, T., Smythe-Wright, D., Sosik, H.M., Thomas, C., Thomas, R., Tilstone, G., Tracana, A., Twardowski, M., Vellucci, V., Voss, K., Werdell, J., Wernand, M., Wojtasiewicz, B., Wright, S., Zibordi, G., 2022. A compilation of global bio-optical in situ data for ocean colour satellite applications – version three. Earth Syst. Sci. Data 14 (12), 5737–5770. http://dx.doi.org/10.5194/essd-14-5737-2022.

van Oostende, M., Hieronymi, M., Krasemann, H., Baschek, B., 2023. Global ocean colour trends in biogeochemical provinces. Front. Mar. Sci. 10, http://dx.doi.org/10.3389/fmars.2023.1052166.

Ward, B.A., 2015. Temperature-correlated changes in phytoplankton community structure are restricted to polar waters. In: Dam, H.G. (Ed.), PLOS ONE 10 (8), e0135581. http://dx.doi.org/10.1371/journal.pone.0135581.

Wei, G., Lee, Z., Wu, X., Yu, X., Shang, S., Letelier, R., 2021. Impact of temperature on absorption coefficient of pure seawater in the blue wavelengths inferred from satellite and in situ measurements. J. Remote Sens. 2021, http://dx.doi.org/10.34133/2021/9842702.

Werdell, P.J., Bailey, S.W., 2005. An improved in-situ bio-optical data set for ocean color algorithm development and satellite data product validation. Remote Sens. Environ. 98 (1), 122–140. http://dx.doi.org/10.1016/j.rse.2005.07.001.

Werdell, P.J., Bailey, S.W., Franz, B.A., Jr., L.W.H., Feldman, G.C., McClain, C.R., 2009. Regional and seasonal variability of chlorophyll-a in Chesapeake Bay as observed by SeaWiFS and MODIS-Aqua. Remote Sens. Environ. 113 (6), 1319–1330. http://dx.doi.org/10.1016/j.rse.2009.02.012.

Werdell, P.J., McKinna, L.I.W., Boss, E., Ackleson, S.G., Craig, S.E., Gregg, W.W., Lee, Z., Maritorena, S., Roesler, C.S., Rousseaux, C.S., Stramski, D., Sullivan, J.M., Twardowski, M.S., Tzortziou, M., Zhang, X., 2018. An overview of approaches and challenges for retrieving marine inherent optical properties from ocean color remote sensing. Prog. Oceanogr. 160, 186–212. http://dx.doi.org/10.1016/j.pocean.2018.01.001.

Westberry, T.K., Boss, E., Lee, Z., 2013. Influence of Raman scattering on ocean color inversion models. Appl. Opt. 52 (22), 5552. http://dx.doi.org/10.1364/AO.52.005552.

Westberry, T.K., Dall'Olmo, G., Boss, E., Behrenfeld, M.J., Moutin, T., 2010. Coherence of particulate beam attenuation and backscattering coefficients in diverse open ocean environments. Opt. Express 18 (15), 15419. http://dx.doi.org/10.1364/OE.18.015419.

Whitmire, A.L., Pegau, W.S., Karp-Boss, L., Boss, E., Cowles, T.J., 2010. Spectral backscattering properties of marine phytoplankton cultures. Opt. Express 18 (14), 15073. http://dx.doi.org/10.1364/OE.18.015073.

Wiegmann, S., Liu, Y., Bracher, A., 2019. Spectrophotometric measurements of absorption coefficients by total particles, phytoplankton and non-algal particles during POLARSTERN cruise PS93.2. http://dx.doi.org/10.1594/PANGAEA.907605.

Xi, H., Losa, S.N., Mangin, A., Garnesson, P., Bretagnon, M., Demaria, J., Soppa, M.A., Hembise Fanton d'Andon, O., Bracher, A., 2021. A data set of collocated satellite remote sensing reflectance from GlobColour merged products, chlorophyll a concentration of phytoplankton functional types derived from in situ pigment data, and CMEMS sea surface temperature from 2002 to 2012. http://dx.doi.org/10.1594/PANGAEA.930087.

Xiu, P., Chai, F., 2014. Connections between physical, optical and biogeochemical processes in the Pacific Ocean. Prog. Oceanogr. 122, 30–53. http://dx.doi.org/10.1016/j.pocean.2013.11.008.

Yu, X., Lee, Z., Wei, J., Shang, S., 2019. Impacts of pure seawater absorption coefficient on remotely sensed inherent optical properties in oligotrophic waters. Opt. Express 27 (24), 34974. http://dx.doi.org/10.1364/OE.27.034974.

Zaneveld, R., Barnard, A., Lee, Z., 2006. Why are inherent optical properties needed in ocean-colour remote sensing? In: Lee, Z. (Ed.), Remote Sensing of Inherent Optical Properties: Fundamentals, Tests of Algorithms, and Applications. Reports of the International Ocean-Colour Coordinating Group, No. 5, IOCCG, Dartmouth, Canada, pp. 3–10.

Zhang, X., Hu, L., 2009. Estimating scattering of pure water from density fluctuation of the refractive index. Opt. Express 17 (3), 1671. http://dx.doi.org/10.1364/OE.17.001671.

Zhang, X., Hu, L., He, M.-X., 2009. Scattering by pure seawater: Effect of salinity. Opt. Express 17 (7), 5698. http://dx.doi.org/10.1364/OE.17.005698.

Zhang, X., Huot, Y., Bricaud, A., Sosik, H.M., 2015. Inversion of spectral absorption coefficients to infer phytoplankton size classes, chlorophyll concentration, and detrital matter. Appl. Opt. 54 (18), 5805. http://dx.doi.org/10.1364/AO.54.005805.

Zhao, J., Cao, W., Wang, G., Yang, D., Yang, Y., Sun, Z., Zhou, W., Liang, S., 2009. The variations in optical properties of CDOM throughout an algal bloom event. Estuar. Coast. Shelf Sci. 82 (2), 225–232. http://dx.doi.org/10.1016/j.ecss.2009.01.007.

Zielinski, O., Voß, D., Henkel, R., Garaba, S.P., Cembella, A., 2013. Chlorophyll a concentration during the during the North Sea Coast Harmful Algal Bloom (NORCOHAB II) HEINCKE cruise HE302. http://dx.doi.org/10.1594/PANGAEA.811777.